Evolution and architecture of an exhumed ocean-facing coarse-grained submarine canyon fill, Baja California, Mexico

MAX J. BOUWMEESTER* (iD), IAN A. KANE* (iD), DAVID M. HODGSON† (iD),
STEPHEN S. FLINT*, WILLIAM J. TAYLOR† (iD), EUAN L. SOUTTER* (iD),
ADAM D. MCARTHUR† (iD), MIQUEL POYATOS-MORÉ‡ (iD), JOSHUA MARSH*,
ED KEAVNEY† (iD), RUFUS L. BRUNT* (iD) and VICTORIA VALDEZ-BUSO§
*University of Manchester, Manchester, UK (E-mail: max.bouwmeester@manchester.ac.uk)
†University of Leeds, Leeds, UK
‡Universitat Autònoma de Barcelona, Bellaterra, Spain
§Universidade Federal do Paraná, Curitiba, Brazil

Associate Editor – Lawrence Amy

ABSTRACT

Present day submarine canyons are active conduits for the transfer of large volumes of sediment, carbon and pollutants from continents to oceans. However, the evolution of submarine canyons over geological timescales remains poorly understood due to their erosional nature and low preservation potential. The Late Cretaceous Punta Baja Formation represents a well-preserved submarine canyon-fill that evolved on a tectonically-active ocean-facing margin. Exposures provide kilometre-scale continuous strike and dip sections of the 120 m thick and 1.2 km wide feature. An inherited tectonic fabric influenced the location and orientation of canyon incision into fluvial bedrock. The stratigraphic evolution of the Punta Baja submarine canyon is reconstructed from incision to fill, which shows that it remained an active sediment conduit throughout the time represented by the preserved fill. The depositional architecture of the north–south oriented erosionally confined canyon-fill is asymmetrical, with sub-vertically stacked channel-fills to the west, and an overbank confined by the canyon margin to the east. Sedimentary process interactions led to depositional patterns that are considered distinct to submarine canyon fills. Dynamic topography generated by mass-wasting processes captured sediment and drove knickpoint development, an autogenic mechanism that modifies sediment delivery to the ocean floor. Widespread upstream dipping surfaces in channel-fills are interpreted as the stratigraphic expression of upstream migrating supercritical-flow bedforms, which played an important role in sediment storage and transport in the canyon. The steep relief and internal topography of canyons leads to complicated and characteristic confined overbank flow behaviour and depositional patterns. This study provides insight into how processes that are observed in modern canyons are selectively preserved through the lifetime of the canyon and construct or destroy stratigraphy on geological timescales.

Keywords Active margin, architecture, Cretaceous, facies, flow processes, strike-slip tectonics.

INTRODUCTION

Submarine canyons funnel large volumes of sediment from continents to oceans via gravity flows (Daly, 1936; Kuenen, 1938; Shepard, 1972; Fildani, 2017; Fisher *et al.*, 2021). More than 9500 submarine canyons mapped along the Earth's continental margins (Harris *et al.*, 2014) are now recognized to play an important role in ocean circulation patterns (Allen & Durrieu De Madron, 2009; Zhu *et al.*, 2010; Nazarian *et al.*, 2021), marine biodiversity (Schlacher *et al.*, 2007; Bianchelli *et al.*, 2010; Vetter *et al.*, 2010; Fernandez-Arcaya *et al.*, 2017), and carbon and pollutant export from shelves to deep water locations (Palanques *et al.*, 2008; Pham *et al.*, 2014; Puig *et al.*, 2014; Hage *et al.*, 2020; Taviani *et al.*, 2023). Despite their size and ubiquity, little is known about how sediment in submarine canyons is stored and transferred into the stratigraphic record on geological timescales. Direct monitoring studies over the last decade are challenging paradigms in submarine canyon sediment dynamics, showing that sediment transport in canyons is more frequent (Heijnen *et al.*, 2022b), powerful (Paull *et al.*, 2018), longer-lasting (Azpiroz-Zabala *et al.*, 2017) and dynamic (Aslam *et al.*, 2018; Lo Iacono *et al.*, 2020; Clare *et al.*, 2023) than previously thought (Normark & Piper, 1991). Observations from modern canyons show a wide range of depositional and erosional bedforms, such as sand and gravel waves (e.g. Wynn *et al.*, 2002; Lastras *et al.*, 2009), cyclic steps (e.g. Cartigny *et al.*, 2011), upstream migrating knickpoints (e.g. Guiastrennec-Faugas *et al.*, 2020), furrows and scours (Lastras *et al.*, 2007) and the role of canyon margin failures in changing sedimentation patterns (e.g. Pope *et al.*, 2022). The preservation potential and stratigraphic expression of these bedforms, and the sedimentological responses to canyon margin failure events in the rock record remain a focus of research (e.g. Hage *et al.*, 2018; Allen *et al.*, 2022).

Subsurface studies reveal stacking patterns and internal architectures (e.g. Almgren & Hacker, 1984; Galloway *et al.*, 1991; Rasmussen, 1994; Hsieh *et al.*, 2020; Su *et al.*, 2020; Fisher *et al.*, 2021; Tian *et al.*, 2021; Li *et al.*, 2022; Wu *et al.*, 2022) but lack the finer-scale sedimentological detail that outcrop studies can provide. However, exhumed submarine canyon fills are rare, particularly from ocean-facing systems, and typically have limited downdip control (Clifton, 1984; Von der Borch *et al.*, 1985; Clifton & Hill, 1987; Advocate *et al.*, 1988; FitzGerald & Gorsline, 1989; Morris & Busby-Spera, 1988; Millington & Clark, 1995; Cronin & Kidd, 1998; Seidler, 2000; May & Warme, 2007; Di Celma & Cantalamessa, 2012; Ito *et al.*, 2014; Dasgupta & Buatois, 2015; McArthur & McCaffrey, 2019; Janocko & Basilici, 2021).

The aim of this study is to document a submarine canyon-fill, the Late Cretaceous Punta Baja Formation, which formed on a tectonically active ocean-facing margin of Baja California, north-western Mexico (Fig. 1; Boehlke & Abbott, 1986). This exceptionally well-preserved canyon-fill presents continuous strike and dip sections, allowing the evolution of the submarine canyon to be reconstructed, from incision, through infill, to burial. Mapping, sedimentary logging, high-resolution photogrammetry and detailed facies descriptions are used to document and interpret architectural elements and depositional environments, and to present a new facies model for submarine canyon-fills.

GEOLOGICAL SETTING

Late Cretaceous–Palaeogene sediments were deposited in the Pacific Ocean-facing forearc basin of the Peninsular Ranges (Beal, 1948; Gastil *et al.*, 1975; Busby *et al.*, 2006). The Peninsular Ranges formed in the Early Jurassic as the intra-oceanic Alisitos Arc (Gastil *et al.*, 1975; Busby *et al.*, 1998, 2006) accreted onto North America, which ended at 105 Ma (Busby *et al.*, 2006; Alsleben *et al.*, 2012) by the oblique subduction of the Farallon plate under North America (Hagstrum *et al.*, 1985). During the Late Cretaceous, transpressional tectonics and magmatism caused regional tilting manifested by uplift in the Peninsular Ranges and subsidence to the west (Fig. 2). This uplift provided sediment for deposition of the fluvial Bocana Roja Formation (Turonian), the deep-marine Punta Baja Formation (Coniacian), the shallow-marine to fluvial El Gallo Formation (Campanian), the deep-marine Rosario Formation (Maastrichtian–Danian) and the volcanic-sedimentary Sepultura Formation (Palaeocene) (Fig. 1) in the west-facing forearc basin onlapping the Peninsular Ranges (Beal, 1948; Gastil *et al.*, 1975).

The Peninsular Ranges supplied the Late Cretaceous sedimentary systems with a range of volcanic, intrusive, metamorphic and sedimentary (carbonate, volcaniclastic and siliciclastic) lithologies, across a short and steep basin margin (Figs 1 and 2). Rapid tectonically-forced

Fig. 1. (A) Location of the study area on the Baja California peninsula, Mexico. (B) Geological map of the Baja California peninsula (simplified from Gastil *et al.*, 1971). Lithologies grouped for the purposes of this study in: pre-batholitic and syn-batholitic rocks of the Peninsular Ranges (blue and pink) that are the bedrock and source of the studied Late Cretaceous sedimentary systems (yellow), and younger deposits (pale yellow and orange). Note that modern sediment conduits (white) drain straight from the Peninsular Ranges into the Pacific Ocean, probably in a similar way to sedimentary systems since the Cretaceous. (C) Upper Cretaceous and Palaeocene stratigraphy of the study area with the duration of magmatism on the peninsula highlighted (Kane *et al.*, 2022), with the Punta Baja Formation canyon fill highlighted in bold.
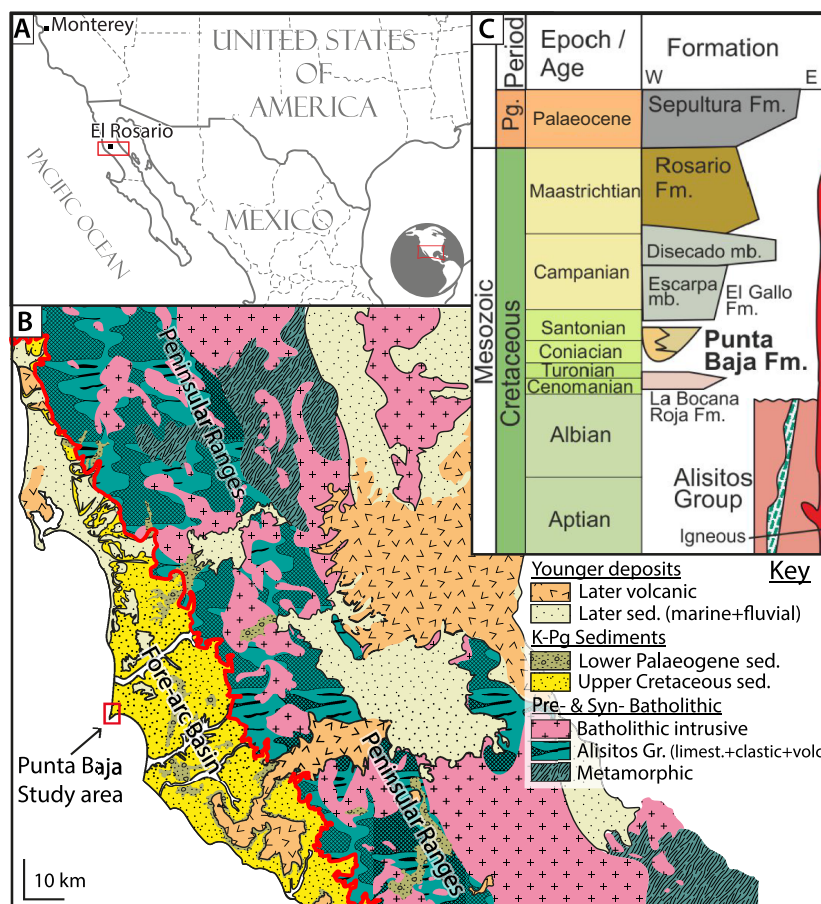
base-level changes (faulting and basinward tilting) controlled the juxtaposition of continental and marine sedimentary systems (Busby *et al.*, 1998; Kane *et al.*, 2022).

The conduit documented in this study is preserved as the Punta Baja Formation submarine canyon-fill, which was incised into the fluvial Bocana Roja Formation bedrock, filled with deep-marine strata, planed off, and onlapped by the shallow-marine El Gallo Formation (Fig. 1), in a timespan of less than 8 Myr (derived from Detrital Zircon dating, Kane *et al.*, 2022). This succession of depositional environments has been described previously (Kilmer, 1963; Schile, 1974; Boehlke & Abbott, 1986; Morris & Busby, 1996; Kane *et al.*, 2022) and is further contextualized below.

La Bocana Roja Formation (Turonian)

The Bocana Roja Formation is the oldest sedimentary unit in the study area [93.6 ± 1.1 Ma Maximum Depositional Age (MDA) derived from
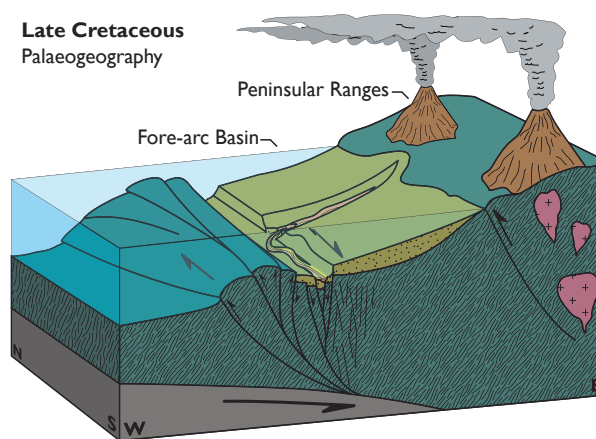

Fig. 2. Schematic palaeogeography during the Late Cretaceous continental arc phase (modified from Busby *et al.*, 1998, and Tsuji *et al.*, 2014) showing the active magmatism and uplift in the Peninsular Ranges, with steep and short sedimentary systems draining and depositing westward into the Pacific Ocean-facing forearc basin, steered by complex structural topography. Colours correspond to Fig. 1B.
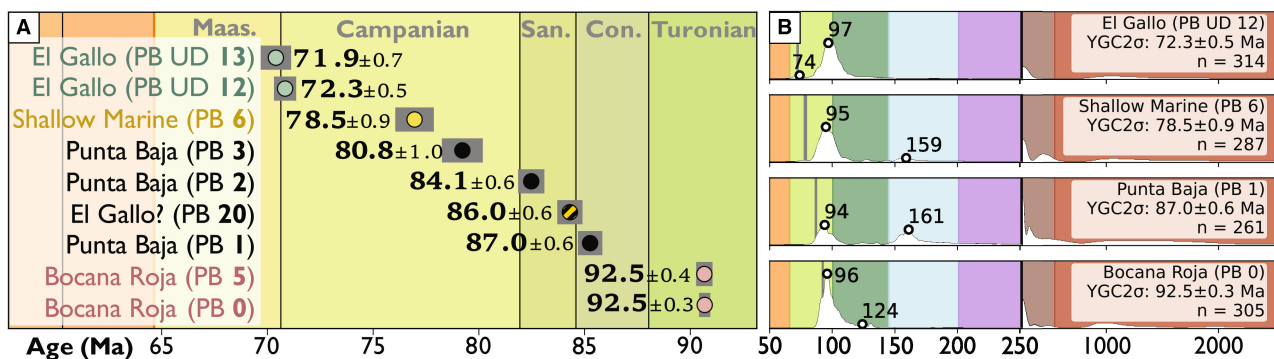
Fig. 3. (A) Large-N Detrital Zircon ages of samples collected from the bedrock Bocana Roja Formation, Punta Baja Formation submarine canyon-fill and shallow marine to fluvial El Gallo Formation. (B) Detrital Zircon age distributions for representative samples with statistically most relevant populations, yielding a Maximum Depositional Age (MDA) using the Youngest Grain Cluster (YGC) 2σ methodology (Dickinson & Gehrels, 2009). Note the change in timescale increments around 250 Ma (Palaeozoic–Mesozoic). Con. = Coniacian, San. = Santonian, Maas. = Maastrichtian.

Large-N Detrital Zircon dating (Fig. 3; Kane *et al.*, 2022)]. The contact with the underlying Alisitos arc is not exposed (Kilmer, 1963; Schile, 1974). The Bocana Roja Formation is a *ca* 675 to 1260 m thick succession of maroon and grey siltstones, sandstones and conglomerates, interpreted as overbank and braided stream deposits in a rapidly subsiding basin, with transport to the south-west (Morris & Busby, 1996). The mudstones are mottled and contain calcrete horizons, indicating palaeosol formation (Morris & Busby, 1996). The sandstones are thick-bedded medium to coarse-grained feldspathic volcanic litharenites, commonly with large trough cross-beds (Schile, 1974) and form 10 m thick single-storey channel-fills interbedded with conglomerate (clast-supported and matrix-supported, cross-bedded to massive) (Morris & Busby, 1996). Abundant black chert clasts and green, brown and purple fine-grained and porphyritic volcanic clasts are common (Kilmer, 1963). The unit is more tectonically deformed than overlying formations, tilted up to 40° to the south on the western margin, and 1° to 18° towards the west on the eastern margin, forming a broad syncline which is heavily faulted, possibly influencing subsequent Punta Baja Formation canyon incision (Kane *et al.*, 2022).

Punta Baja Formation (Coniacian – Santonian)

The Punta Baja Formation basal surface truncates the Bocana Roja Formation and incises steeply into it by at least 140 m, forming a SSW–NNE trending depression 1.2 km wide (Boehlke &

Abbott, 1986; Kane *et al.*, 2022). The infill (87.1 ± 1.5 Ma MDA, Fig. 3; Kane *et al.*, 2022) is dominated by pebble–cobble conglomerate deposits on the western margin, with large clasts of the underlying Bocana Roja Formation bedrock overlying the basal surface (Kane *et al.*, 2022). To the east, these conglomerates grade through wedge-shaped sandstone bodies into thin-bedded turbidites that onlap the erosive surface in the east (Kane *et al.*, 2022). Macropalaeontology and micropalaeontology suggest depositional environments beyond the shelf-edge (Kane *et al.*, 2022). These deposits have been interpreted as channel cut-and-fill, overbank and crevasse-splay deposits of a submarine canyon through which sediment was transported towards the SSW (Boehlke & Abbott, 1986; Morris & Busby, 1996; Kane *et al.*, 2022). Conglomerate clasts are well-rounded and consist predominantly of metamorphosed, silicified intermediate volcanics, and related volcaniclastics and siliciclastic deposits most likely derived from the Alisitos Formation (>25 km distance), with minor quartzite clasts from a terrane further to the east (>100 km distance; Boehlke & Abbott, 1986). A change in source area for the Punta Baja Formation compared to the Bocana Roja Formation is suggested by an increase in metamorphic and quartzite clasts and slightly different detrital zircon signatures (Kane *et al.*, 2022). The strata are tilted uniformly 2° to 5° to the ESE, with local dips of up to 30° due to sedimentary onlap of the canyon wall (Boehlke & Abbott, 1986; Kane *et al.*, 2022). The Punta Baja Formation is less tectonically deformed than the Bocana Roja Formation, but displays several

syn-depositional faults trending NNE–SSW (Kane *et al.*, 2022).

El Gallo Formation (Santonian – Maastrichtian)

The El Gallo Formation overlies both the Bocana Roja and Punta Baja formations with an angular unconformity (Fig. 1C), interpreted as a ravinement surface in the Punta Baja area (Kane *et al.*, 2022). The basal surface is locally overlain by a transgressive cobble lag with bored clasts overlain by shallow-marine sandstones and conglomerates (Kane *et al.*, 2022). Farther east (20–50 km), the El Gallo Formation directly onlaps the Alisitos arc (Kilmer, 1963). The El Gallo Formation (86.8 ± 1.8 Ma MDA, Fig. 3; Kane *et al.*, 2022) has a maximum thickness of 1.3 km and is subdivided (Fig. 1C) into the La Escarpa Member (alluvial fan to braided stream deposits), overlain by the tuffaceous El Disecado Member (fluvial to tidal deposits) that grades eastward into the poorly-sorted conglomeratic El Castillo Member (Kilmer, 1963; Schile, 1974; Morris & Busby, 1996; Fastovsky *et al.*, 2020). Conglomerates in this unit contain mainly rhyolitic, andesitic, granitic and dolerite clasts (Schile, 1974).

METHODS

The Punta Baja Formation canyon fill is exposed around the hamlet of Punta Baja (29°57′20.8″N 115°48′25.0″W) and in coastal cliffs around the Punta Baja peninsula. Desert climate conditions facilitate a general lack of vegetation, which combined with the juxtaposition of well-cemented conglomerates with less-cemented sandstones and mudstones, contribute to excellent continuous exposures. Modern marine terraces are present across the field area, and can be distinguished by their (sub-) horizontal bedding orientation and abundant recent shell material. Recent semi-consolidated to unconsolidated sand dunes overlie bedrock in places. The northernmost coastal part of the field area could not always be accessed or photographed with Uncrewed Aerial Vehicles (UAVs) due to considerations with the local inhabitants.

Mapping and sedimentary logging

Lithostratigraphic and facies-mapping data in the 2.5 × 5.0 km study area were collected using a handheld GPS (Garmin GPSMAP 62s; Garmin, Olathe, KA, USA), the ArcGIS Field Maps (v22.4.2) application, the FieldMOVE Clino Pro (v2.5.19) application, and geological compass and was collated and processed in ArcGIS software. Sedimentary and stratigraphic characteristics were recorded by measuring sections at 1 : 12.5 to 1 : 50 scale, systematically recording bed thickness and boundary surface type, median grain size and texture, conglomerate clast orientation and conglomerate median-largest clast size, sedimentary and diagenetic structures, bioturbation type and degree, palaeocurrent indicators from clast imbrication, ripple foresets, flutes and grooves. A stratigraphic thickness of 450 m was measured across 41 logs. Correlations of surfaces and stratigraphic intervals were achieved by walking out these features where possible, aided by UAV imagery where necessary. A DJI Phantom 2 Pro UAV and DJI Mavic Mini 2 UAV (DJI, Shenzhen, China) were used to collect aerial photographs, with which 2.3 km^2 of detailed three-dimensional outcrop models were constructed using photogrammetry software Agisoft Metashape standard (v1.8.5) and professional (v.2.0.1). All models are available on V3Geo (see Supporting Information).

Palaeocurrent reconstructions (Supporting Information) are presented in equal-area rose diagrams (Nemec, 1988) and subdivided per indicator type (Python code in Supporting Information). Stratigraphic cross-sections are based on elevation profiles derived from our combined UAV 3D outcrop model Digital Elevation Model (DEM, resolution down-sampled to 5 m), mapping and measured sections.

Structural geology

The orientations of fault planes were measured using a geological compass, with their location, trace and apparent offset recorded using the FieldMOVE Clino application and the ArcGIS Field Maps application. Where possible, fault kinematics and net displacements were derived directly from offset stratigraphy, drag folds, shear along fault planes and slickensides. Where fault offsets were unclear or complex, the orientations of conjugate fault sets were recorded to assess for Riedel-shear sense-of-slip indicators. Because the surface expression of most major fault zones in the field area could be explained by pure strike-slip, pure vertical motion, or a combination of the two, both components are indicated on the map without detailing the relative contributions of strike-slip and vertical motion. The orientations of

fault planes were analysed per formation (Bocana Roja or Punta Baja formations), type (normal/ reverse or transform) and location (north-west or south-east). The data (Supporting Information) were plotted using Stereonet 11 software (Allmendinger *et al.*, 2013; Cardozo & Allmendinger, 2013) on equal-area stereonets as poles to fault planes, after which clustering was determined using Kamb's contouring (Kamb, 1959). The data were filtered according to these variables to derive the signature of each in the complete dataset (Supporting Information). Planes to clusters in the dataset were fitted to derive mean fault orientations. The dominant fault characteristics are then carried over to the bigger groupings of data (Fig. 4).

Stratigraphic statistics

Beds were assigned to facies and facies associations, and their recorded characteristics grouped and analysed accordingly. Logged facies, grain-size and bed thickness (classified according to Campbell, 1967) characteristics were plotted as Kernel Density Estimates (KDE) of number of beds to represent the entire dataset, with the mean, 5th percentile and 95th percentile extracted as summary statistics. Representative facies distributions within each facies association were calculated by stratigraphic thickness. The ratio between coarse (very fine sand and coarser) and fine-grained (silt and finer) sediment was calculated per measured section and per environment, scaled by stratigraphic thickness. The coarse–fine values of heterolithic facies were estimated in the field based on sand-to-mud thickness ratio.

Since averaged coarse–fine ratios carry no information on the distribution of lithologies within any given interval, an alternative parameter representing heterogeneity has been developed. Heterogeneity is defined here in a purely vertical stratigraphic sense, by the number of changes between coarse and fine lithologies per metre of measured stratigraphy (changes

per metre or c/m). Together with the averaged coarse–fine ratio values, this characterizes facies and environments in a way that can be applied to subsurface settings.

Photogrammetric model analysis

The orientation of surfaces was calculated from high-resolution 3D outcrop models in LIME software (Buckley *et al.*, 2019) (Supporting Information). A plane was fitted using Singular Value Decomposition (SVD), which yielded a dip direction, dip angle, spatial coordinates of the centre point and point cloud maximum diameter (Python code and data in Supporting Information). From all measured surfaces ($n = 631$), obvious non-planar surfaces and steep erosional features marked during interpretation were excluded to yield 539 sedimentary surfaces. These were plotted on a map and their dip and dip direction were compared to the mean palaeocurrent direction in the canyon derived from conglomerate clast imbrication (south-west). Post-sedimentary tectonic tilting in the study area is minimal. The orientation of adjacent thin-bedded overbank deposits, which are now tectonically tilted by 2° to 5° to the ESE, are assumed to approximate palaeo-horizontal surfaces. Due to the low tectonic dip (<5°) and consistent dip direction, the palaeocurrent measurements were not restored.

Detrital zircon dates

Two samples for large-N Detrital Zircon dating were collected to complement the previously published dataset of Kane *et al.* (2022). Detrital Zircons for both studies were extracted and processed at the University of Calgary. Uranium/lead ratios and dates of three hundred grains from each sample ($n = 9$) were obtained using Laser Ablation – Inductively Coupled – Plasma Mass Spectrometry (LA–ICP–MS) following the methodology of Matthews & Guest (2016).

Fig. 4. Lithostratigraphic formations and facies map of the field area with major fault traces, location of cross-sections in Fig. 9 and equal-area rose diagram of palaeocurrent indicators. Fault kinematics on traces on the map are displayed with vertical and lateral components that could explain the outcrop pattern, however the exact kinematics are unknown. Fault plane orientations plotted on stereographs as poles and grouped per type, formation and location. In the north-west of the field area, the Bocana Roja subcrop is normally faulted to the south-west with a strike-slip component trending south-west. The Punta Baja Canyon fill in the north-west is transform faulted trending SSW, parallel to palaeoflow, indicating a link between sediment transport direction and tectonic regime. In the south-east of the field area the Bocana Roja subcrop is normally faulted towards the NNE, which is antithetic to the north-west normal faults. The Punta Baja Canyon fill in the south-east is transform faulted trending north-west, perpendicular to palaeoflow and the western transform fault system.
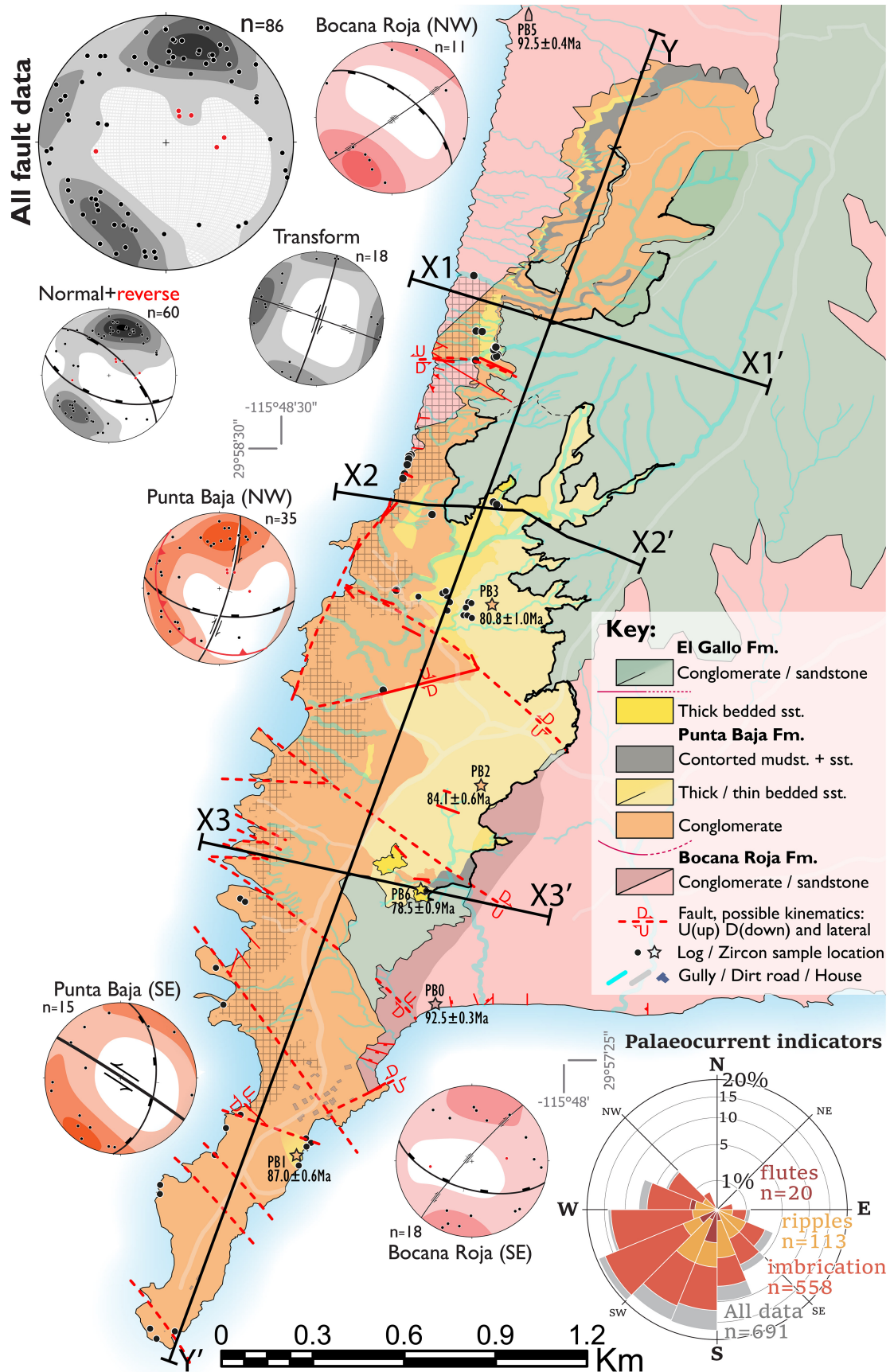
Sandstone maximum depositional ages (MDAs) were (re-)calculated using the Youngest Grain Cluster (YGC) 2σ methodology (Dickinson & Gehrels, 2009) and analysed using a modified version of detritalPy (Sharman *et al.*, 2018) (Fig. 3). Where possible, the youngest detrital zircon grains were re-ablated to test the isotopic homogeneity of the grain(s) used in the calculation of the MDA and to reduce uncertainty (Spencer *et al.*, 2016).

Micropalaeontological and palynological data

Micropalaeontological ($n = 2$) and palynological ($n = 2$) samples were collected to compare with those documented in Kane *et al.* (2022) and processed in a standard fashion (Wood *et al.*, 1996). Residues were analysed for their organic matter content and identification of key dinoflagellate cyst species. Species were compared with published regional age ranges to determine an acme age range and depositional environment.

RESULTS

Structural geology

Structural pattern of study area
Structural deformation in the study area is dominated by normal faults, dipping $60° \pm 10°$ to the SW or NNE (Fig. 4). Strike-slip faults occur generally as near-vertically dipping ($80°$ to $90°$) NNE–SSW trending fault zones, and more rarely trending in a perpendicular WNW–ESE direction (Fig. 4). Reverse faults are rare ($n = 6$), generally dipping $30°$ to $40°$ to the north-east (Fig. 4). The perpendicular orientation of strike-slip and normal-reverse faults in the study area is consistent with a locally extensional transform stress regime, often seen in releasing bends or stepover zones in transform systems (Reading, 1980; Rodgers, 1980; Christie-Blick & Biddle, 1985; Wu *et al.*, 2009; Huang & Liu, 2017).

The sense of movement along strike-slip faults is difficult to establish in the field, without clear indictors such as slickensides or offset lithological boundaries. The analysed conjugate fault sets and the measured orientations were incompatible with Riedel shearing (i.e. markedly different to $15°$ R1 or $75°$ R2: Rutter *et al.*, 1986; Dresen, 1991; Misra *et al.*, 2009). This is attributed to the rheology of coarse sandstones and conglomerates, or the oblique-slip stress regime (Katz *et al.*, 2004). Compatible orientations

tentatively indicate a dextral strike-slip sense for north-east/south-west trending faults, which agrees with the regional stress regime related to the oblique subduction and northward translation of the arc terrain relative to North America.

Subcrop deformation
The Bocana Roja Formation subcrop that underlies the Punta Baja canyon-fill is dominantly normal faulted, with antithetic $60°$ dipping fault planes. The dominant fault displacement direction in the north-west of the study area is towards the south-west (normal faults), while on the opposite side of the canyon fill in the south-east, the displacement direction is dominantly to the north-east (normal faults) (Fig. 4). This antithetic spatial distribution of extensional faults is interpreted to represent opposing extremities of a releasing bend (Kane *et al.*, 2022). The south-west/north-east trending dextral strike-slip lineament and the extensional normal faults in the Bocana Roja Formation bedrock forming in a releasing bend of a transform zone likely steered and accommodated the Punta Baja canyon as a conduit. This explains the SSW-directed sediment transport within the canyon (Fig. 4), which diverges from the regional westward trend of sedimentary systems that is perpendicular to the palaeo-slope (Figs 1 and 2) (Kane *et al.*, 2022).

Canyon fill deformation
The strike-slip faults in the Punta Baja canyon-fill trend SSW–NNE, at a slight angle with the south-west/north-east trending faults in the Bocana Roja Formation subcrop (Fig. 4). This difference might be due to rotation of the Bocana Roja Formation caused by the ongoing transform faulting during Punta Baja Formation deposition. This rotation could be accommodated in rotational blocks documented in transform shear zones and releasing/constraining bends (Christie-Blick & Biddle, 1985). The north-west/south-east trending transform fault signature in the study area likely represents the shear zones that bound the rotational blocks, consistent with the sinistral sense of shear observed in some of these fault zones.

The reverse faulting in the northern segment of the Punta Baja canyon-fill is directed southwestward and might indicate either tectonic inversion in the northern section of the releasing bend, or syn-depositional down-slope failure and the compressional 'toe' of mass wasting of the canyon deposits. Normal faulting in the south-east segment of the Punta Baja canyon-fill might represent sedimentary failure of canyon deposits into the

Table 1. Facies descriptions and statistics, with reference to Fig. 5 for representative photographs.

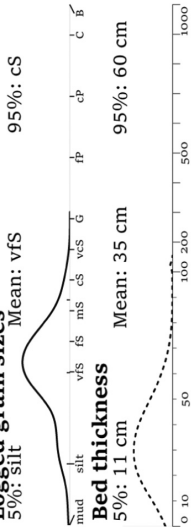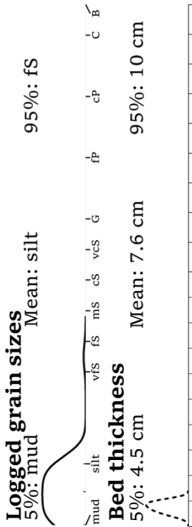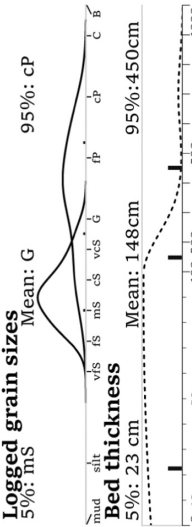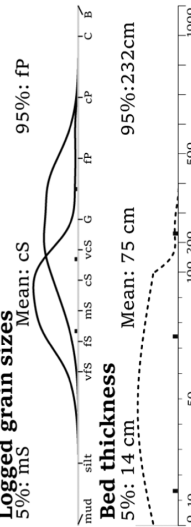| Code	Name	Statistics	Description	Interpretation	Figure 5
Fm	Massive mudstone	**Logged grain sizes** 5%: mud; Mean: mud; 95%: silt. **Bed thickness** 5%: 2 cm; Mean: 10 cm; 95%: 27 cm	Massive structureless mudstone, commonly rich in sub-millimetre scale organic material	Deposits from hemipelagic suspension fallout, or low-concentration turbidity currents that are too fine-grained to differentiate by the naked eye (Boulesteix *et al.*, 2019)	A
Fl	Laminated mudstone	**Logged grain sizes** 5%: mud; Mean: mud; 95%: vfS. **Bed thickness** 5%: 4 cm; Mean: 21 cm; 95%: 70 cm	Laminated mudstone and siltstone, continuous or discontinuous laminae, common millimetre-scale organic material	Deposits from low-concentration turbidity currents (Bouma, 1962; Mutti, 1992; Boulesteix *et al.*, 2019)	B
H	Heterolithics	**Logged grain sizes** 5%: mud; Mean: fS / mud; 95%: mS. **Bed thickness** 5%: 7.5 cm; Mean: 41 cm; 95%:120cm	Thin-bedded alternations of mudstone and sandstone, commonly planar laminated. Laminated to ripple cross-laminated	Sedimentation by low-concentration turbidity currents, resulting from the more dilute parts of gravity flows, or unidirectional transitional flows (Taylor *et al.*, 2024a). Alternatively, could record reworking by internal tides (Puig *et al.*, 2004; Li *et al.*, 2019; Normandeau *et al.*, 2024)	C,D
ST	Turbidite sandstone	**Logged grain sizes** 5%: mud; Mean: fS-mS / silt; 95%: fP. **Bed thickness** 5%: 2.5 cm; Mean: 21 cm; 95%: 70 cm	Medium to thick-bedded sandstones and siltstones, dominantly normally graded, massive or planar laminated to ripple laminated. Common mudclasts and outsized clasts	Sedimentation from high-concentration and low-concentration turbidity currents	E

Table 1. (continued)

Code	Name	Statistics	Description	Interpretation	Figure 5
Sl	Low-angle cross-laminated sandstone	**Logged grain sizes** 5%: silt, Mean: vfS, 95%: cS; **Bed thickness** 5%: 11 cm, Mean: 35 cm, 95%: 60 cm	Medium to thick-bedded sandstone with low-angle cross-lamination, commonly truncations in multiple directions and diverging/converging laminations	Deposition from supercritcal turbidity currents (Komar, 1971; Hand, 1974; Postma & Cartigny, 2014), hummock-like and swale-like geometry possibly due to combined flow dynamics due to seabed topography (Harms, 1969; Tinterri, 2011; Taylor *et al.*, 2024a)	F
Sw	Wave-rippled sandstone	**Logged grain sizes** 5%: mud, Mean: silt, 95%: fS; **Bed thickness** 5%: 4.5 cm, Mean: 7.6 cm, 95%: 10 cm	Sandstone and siltstone with symmetrical cross-laminations. Sideritic concretions and organic material common	Sedimentation from oscillatory flow above fair-weather wave-base	G
Dm	Mudclast breccia	(No statistics)	Angular mudclasts in a matrix of sandstone or mudstone, clast-supported or matrix-supported. Clasts may be oriented sub-horizontally or imbricated	Product of the erosion of poorly lithified, but consolidated, mud-rich sediments. Limited transport distance	I
CSh	Horizontally interstratified conglomerate and sandstone	**Logged grain sizes** 5%: mS, Mean: G, 95%: cP; **Bed thickness** 5%: 23 cm, Mean: 148cm, 95%:450cm	(Sub-)Horizontally stratified conglomerate and sand couplets	Produced by high-concentration turbidity currents, multiple pulses either within a single event or within multiple events (Cronin, 2018)	J
CSx	Cross-stratified conglomerate and sandstone	**Logged grain sizes** 5%: mS, Mean: cS, 95%: fP; **Bed thickness** 5%: 14 cm, Mean: 75 cm, 95%:232cm	Dune-scale cross-stratified conglomerate and sand couplets	Dune gravel bedforms or gravel bar deposits, resulting from high-concentration turbidity currents tractionally reworking or transporting clasts forming dunes or sediment waves (Cronin, 2018) or migrating bars	J,K,L,M

Table 1. (continued)

| Code	Name	Statistics	Description	Interpretation	Figure 5
Co	Organized conglomerate	**Logged grain sizes** 5%: G Mean: fP 95%: C **Bed thickness** 5%: 9 cm Mean: 82 cm 95%: 300cm	Clast-supported conglomerate with a preferred clast fabric. Normal or inverse graded. Occasionally cross-stratified	Non-cohesive debris flow (Lowe, 1982; Postma *et al.*, 1988; Cronin, 2018). Inverse grading when dispersive pressure is high at base of flow, normal grading when dispersive pressure lower (Walker, 1975). Reworking by bedload transport and possibly generating gravel bars or gravel waves (Piper & Kontopoulos, 1994; Wynn et al., 2002; Ito & Saito, 2006)	N,O
Cu	Unorganized conglomerate	**Logged grain sizes** 5%: vcS Mean: fP 95%: C **Bed thickness** 5%: 11 cm Mean: 105 cm 95%: 295cm	Clast-supported or matrix-supported poorly-sorted conglomerate with a high poorly-sorted matrix content. Normally, inversely or non-graded	Grain flow or *en masse* freezing of flow (Walker, 1975), related to local failure and short-runout transport of oversteepened deposits with non-cohesive debris-flow characteristics (Nemec, 1990; Cronin, 2018)	N,O
	Slump/slide	(No statistics)	Rotated to plastically deformed deposits	Slope failure with coherent behaviour: short transport distance, immature mass-transport deposit	P
	Debrite	(No statistics)	Mud-rich intervals with disintegrated bedding	Slope failure with complete disaggregation: longer transport distances, mature mass-transport deposit	H,Q
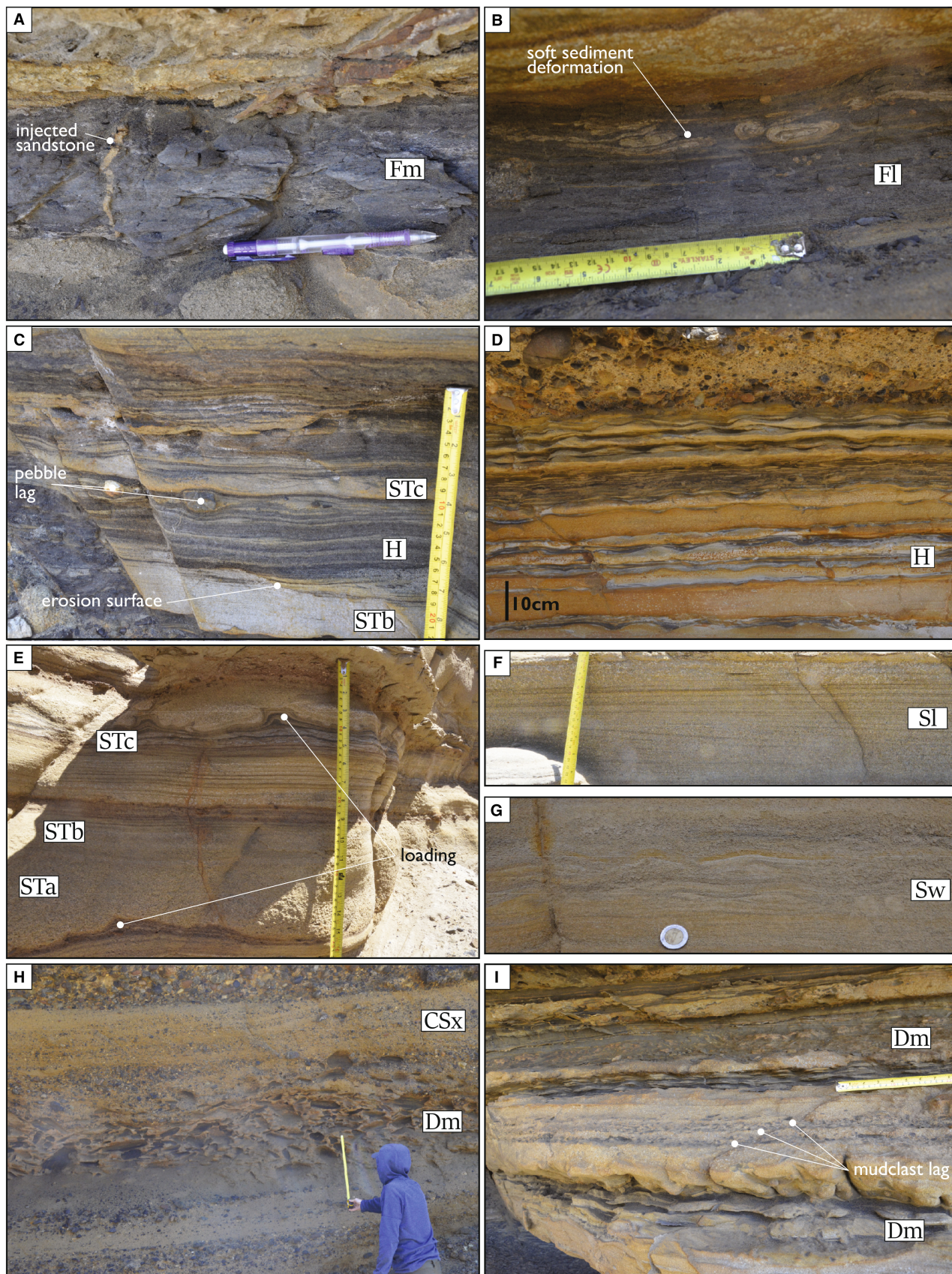
Fig. 5. Representative field photographs of facies in Table 1. (A) Massive mudstone (Fm) with small-scale sandstone injectite. Pencil is 15 cm long. (B) Laminated mudstone (Fl) with soft sediment deformation structures in overlying deposit. (C) Heterolithic interval ('H') with minor sandstone in mudstone, overlying planar laminated turbidite sandstone (STb) and overlain by ripple laminated sandstone (STc). (D) Heterolithic interval ('H') of thin-bedded turbidite sandstones showing clear ripple lamination interbedded with mudstones in varying proportions. (E) Turbidite sandstones (ST) with centimetre-scale load-structures where their bases are in contact with mudstones. (F) Low-angle cross-laminated sandstone (Sl). (G) Symmetrical-ripple laminated sandstone (Sw) showing climbing cross-lamination. Coin is 210 mm in diameter. (H) Thick interval of mudclast breccia (Dm) with coarse sand matrix overlain by cross-stratified conglomerate and sandstone (CSx) dominated by sandstone. (I) Thin intervals of mudclast breccias (Dm) and mudclast lags. (J) Cross-stratified conglomerate and sandstone (CSx) dominated by conglomerate overlain by horizontally interstratified conglomerate and sandstone (CSh). Person for scale is *ca* 1.8 m tall. (K) Cross-stratified conglomerate and sandstone (CSx) with equal proportions conglomerate and sandstone. (L) Steeply cross-stratified conglomerate and sandstone (CSx) dominated by sandstone. (M) Sigmoidal cross-stratified conglomerate and sandstone (CSx) dominated by sandstone with imbricated mudstone clasts on the foresets. Lens cap is 67 mm in diameter. (N) Unorganized conglomerate (Cu) overlain by clasts of Bocana Roja canyon substrate and organized conglomerate (Co) with clear clast imbrication indicating palaeoflow direction towards the left of the picture. (O) Inverse and normal grading in conglomerates. (P) Debrite (deb) overlain by a sandstone bed and slumped thin-bedded turbidites. (Q) Mud-rich debrite. Markings on the pole are 10 cm increments.

conduit due to sedimentary oversteepening or tectonic activity. No definitive indicators to differentiate the syn-depositional from post-depositional nature of these faults were recognized.

Facies and depositional environments

Submarine canyon axis – submarine channel braid-plain deposits

Description: This facies association is up to 30 m thick, overlies a basal erosion surface, and is characterized by thin to thick-bedded highly amalgamated conglomerates and sandstones, with minor heterolithic intervals (<3 m thick). This facies association has the lowest mud content by stratigraphic thickness and is the most homogeneous. The succession is dominated by thick-bedded organized (Co) and disorganized (Cu) conglomerates (Table 1; Fig. 5N and O), commonly with erosive bases and/or within successions confined by steep erosion surfaces (Fig. 6A and B). Cross-bedded conglomerate or interbedded conglomerate–sandstone (CSx) (Table 1; Fig. 5J to M) is found in tabular packages up to 2 m thick (Fig. 6C), or as wedges that commonly overlie mudclast breccia (Dm) (Table 1; Fig. 5I) that form concave-up lenses (Fig. 6D). Sub-horizontal interstratified conglomerates and sandstones (CSh) (Table 1; Fig. 5J) provide the most laterally continuous beds of the facies association, with minor variations in bed thickness along their length (Fig. 6C). These facies may be truncated by metre-scale erosion surfaces overlain by massive sandstone (ST) (Table 1; Fig. 5E) with minor gravel lags (Fig. 6E). Thinner-bedded sandstone (ST) and heterolithics (H) overlie and onlap conglomerates in fining-upward and thinning-upward successions up to 3 m thick.

Interpretation: This facies association is interpreted as submarine braid-plain deposits (Hein, 1984; Klaucke & Hesse, 1996; Hesse *et al.*, 2001). Conglomerate deposition on the submarine braid plain was governed by non-cohesive debris flows (Walker, 1975; Lowe, 1982; Postma *et al.*, 1988; Cronin, 2018) eroding and delivering gravel *en masse* (Walker, 1975) and tractional reworking by turbidity currents (Cronin, 2018). Non-cohesive granular debris flows may have originated from failure of oversteepened slopes and eroded the seafloor (Dakin *et al.*, 2013), resulting in steep truncation surfaces.

Tractional reworking of gravel on the canyon floor by overriding sediment gravity flows resulted in more organized, sorted and structured conglomerate deposits. Conglomerates preserve clast imbrication in channel thalwegs, which requires sustained high flow velocities for bedload transport. Cross-bedded and well-sorted conglomerates or conglomerates–sandstones represent accretion surfaces of migrating mid-braid-plain or bank-attached bars (Klaucke & Hesse, 1996; Hesse *et al.*, 2001). Horizontally interstratified conglomerate–sandstone is formed by traction carpets (Lowe, 1982; Cronin, 2018). These features could constitute parts of large depositional bedforms beyond the scale of observation, such as gravel waves (Hein, 1984; Piper & Kontopoulos, 1994; Wynn *et al.*, 2002; Ito & Saito, 2006) or cyclic steps. The metre-scale truncation surfaces represent scours, furrows, grooves, cut-off channels and other erosional bedforms filled by sand and gravel from subsequent flows.
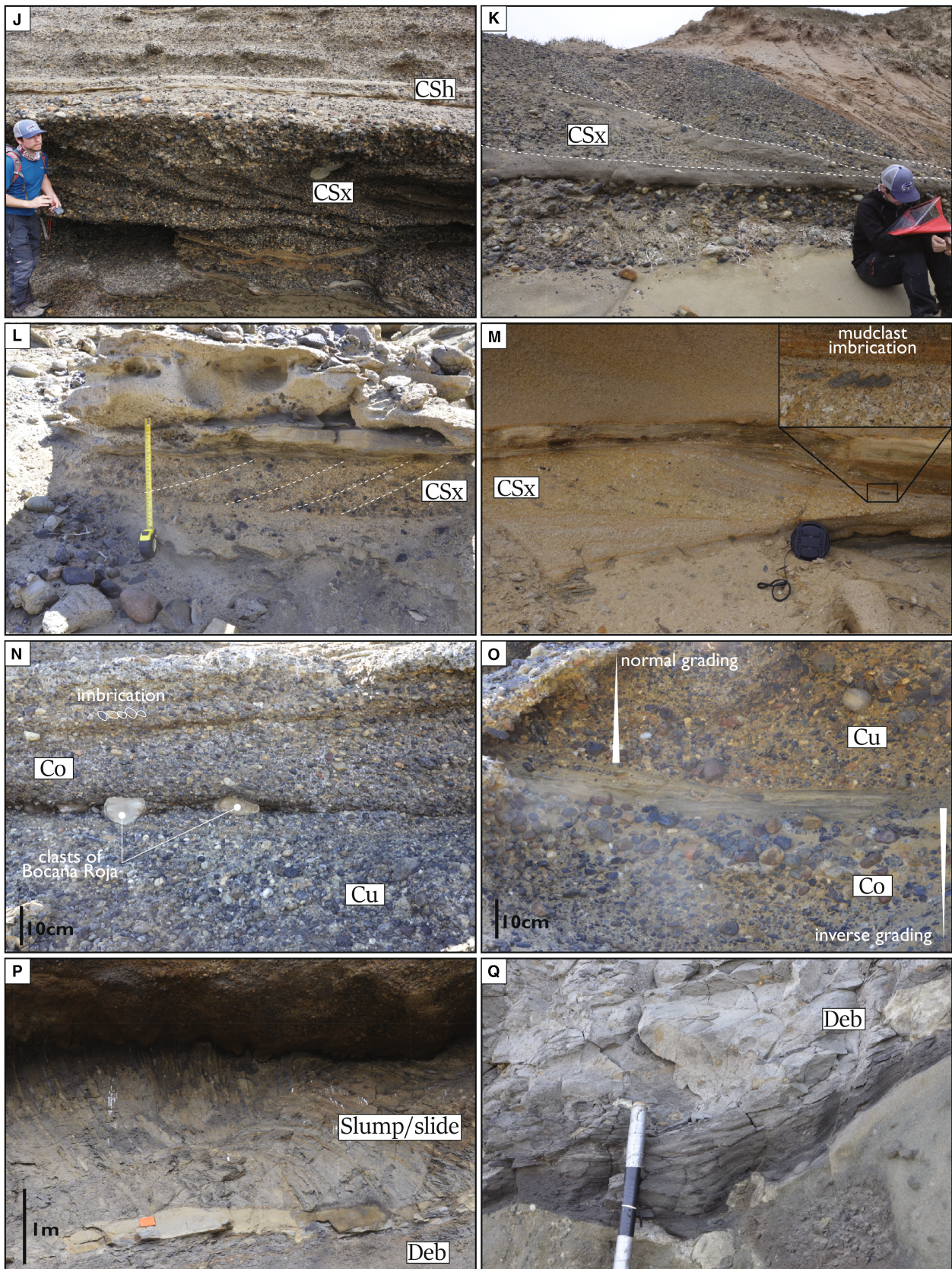
Fig. 5. Continued.

Sandstone is generally underrepresented in braid-plain deposits. This is attributed to the strongly bypassing nature of turbidity currents that likely reworked the gravel deposits. Turbidity currents that deposited sand and mud on the braid plain are preserved as scour-fills, which were shielded by their negative relief. Evidence for fine-grained deposition on the braid plain comes in the form of abundant sandstone rafts, mudclast-rich sandstones and mudclast breccias found in axial deposits. These represent the erosional products of (semi-)consolidated deposits, transported over limited transport distances.

Submarine canyon axis – submarine channel margin deposits

Description: Channel margin facies association deposits are up to 15 m thick and characterized by thick to thin-bedded sandstones (ST), with heterolithics (H; <1 m thick) and minor conglomerates (CSx; <1 m thick) (Table 1; Fig. 5). Commonly, beds are normally graded and stack in generally fining-upward and thinning-upward successions, with a stratigraphic decrease in bed amalgamation. The channel margin facies association typically overlies erosion surfaces that cut into channel axis deposits. Beds appear tabular in dip section, but thin and fine eastward in strike section to onlap metres deep westward-dipping truncation surfaces. Locally, debrites (Table 1; Fig. 5H and Q) overlie these surfaces, which are in turn onlapped by sandstones (ST; Table 1; Fig. 5E). Conglomeratic divisions with load structures are common at bed bases (Fig. 7A), which can be planed-off and completely separated from conglomerate beds (Fig. 7B). Sandstones often display dewatering structures, such as pipe structures and load balls (Fig. 7C). Commonly, current ripple lamination is climbing, forms mixed grain-size bedforms (*sensu* Taylor *et al.*, 2024a) (Fig. 7D), and records a south-east-directed palaeoflow direction. Folded heterolithics, mudclast breccia and debrites are common, in various stages of disaggregation (Figs 6F, 6G and 7C). A thicker interval (*ca* 15 m thick) of amalgamated debrites and slumps is preserved in the north of the field area. Overlying medium to thick-bedded turbidites (ST) with common low-angle (<10°) cross-bedding (Sl; Table 1; Figs 5F and 7E) and a variety of ripple types and palaeocurrent directions onlap depositional relief. Vertical paired *Tisoa* burrows are found in debrites below erosion surfaces.

Interpretation: These deposits formed in a transitional region between the axis and the overbank, and their relationship with overlying, and

onlapping, metres scale erosion surfaces supports a channel margin interpretation. Deposition was by turbidity currents lateral to the highest-energy parts of flows in the axis. Abundant dewatering structures and climbing ripples with varying mud content suggest high rates of deposition under rapidly decelerating flows (Baas *et al.*, 2011; Taylor *et al.*, 2024a). Detached conglomeratic load-balls (Fig. 7B) support transient high energy conditions and high degrees of sediment bypass. Fining-upward and thinning-upward successions are related to channel abandonment, and to healing of depositional relief.

Low-angle (<15°) cross-bedding observed in thick-bedded sandstones of this facies association is localized around erosional and depositional relief. This supports an interpretation of flow reflection and deflection off of local topography forming bedforms (e.g. Hiscott & Pickering, 1984; Kneller *et al.*, 1991). Similar flow-topography interactions are held responsible for the varying nature and migration direction of ripples in thinner-bedded turbidites near these confining surfaces (Hiscott & Pickering, 1984; Kneller *et al.*, 1991; Edwards *et al.*, 1994). The denser, coarser-grained flows, or parts of flows, which deposited the low-angle cross-bedded thick beds carried more momentum and were thus less affected by the topography than the more dilute, finer-grained flows, or parts of flows, which deposited the thin-bedded ripple laminated turbidites.

Submarine canyon overbank

Description: The overbank facies association forms thin to medium-bedded heterolithic successions with varying sandstone to mudstone ratios (Fig. 8), and common thinning-upward and fining-upward packages. Typically, the overbank facies association conformably overlies axial and channel margin deposits, or locally abruptly overlies slumped beds. Rare medium-bedded sandstones form outsized beds with dune-scale cross-bedding and depositional relief (Fig. 7F). Pebble-grade lag deposits (Fig. 7A) and flat-topped coarse-grained sandstone to gravel lenses (Fig. 7G) are concentrated towards the western extent of this facies association. Shallow-angle erosion surfaces are common and overlain with sandstone (Fig. 7H). Typically, sandstones (ST; Table 1; Fig. 5E) are parallel to ripple cross-laminated. Ripple types include steep climbing, mixed grain-size (high-amplitude with mud-rich troughs and low amplitude) and starved ripple trains (Fig. 7I), which are associated with starved laminae (Taylor *et al.*, 2024a). Palaeocurrent directions are variable but
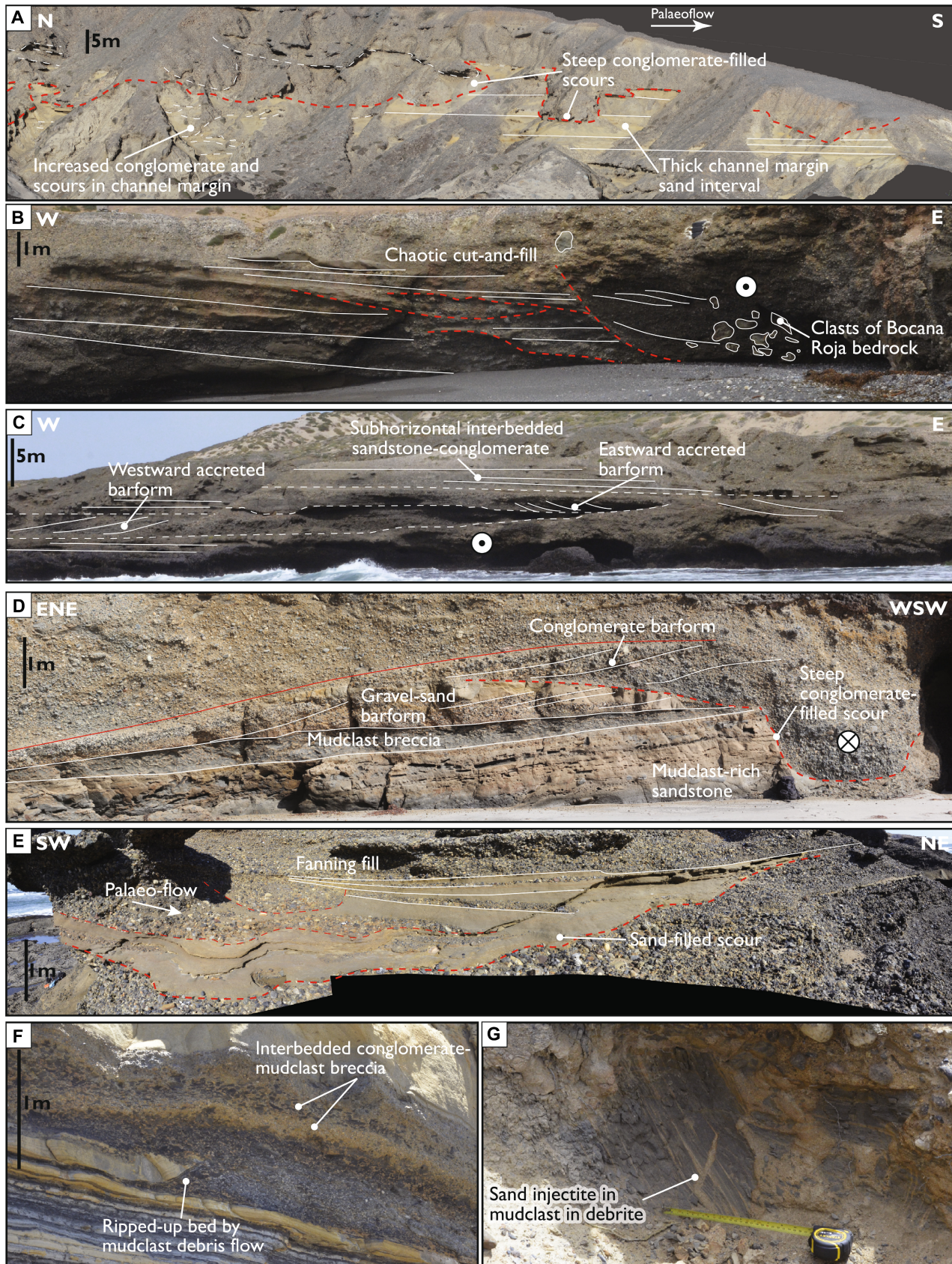
Fig. 6. Field photographs representing depositional and erosional bedforms in coarse-grained deposits. (A) Thick (*ca* 20 m) interval of channel margin sandstones steeply truncated by channel axis conglomerates. (B) Several erosion surfaces in conglomeratic braid-plain deposits, overlain by conglomerate with metre-scale clasts of Bocana Roja canyon bedrock. (C) Large-scale cross-bedded conglomerates with accretion directions perpendicular to palaeoflow (out of page), suggesting laterally accreting bars on the canyon floor. (D) A succession of mudclast-rich sandstone, mudclast breccia, cross-bedded conglomerate and sandstone steeply truncated and overlain by unorganized and cross-bedded conglomerate. (E) Metre-scale sand-filled scour with fanning geometry in conglomeratic braid-plain deposits. (F) Turbidite sandstone bed that has been deformed, truncated and partially encased in mudclast breccia, suggesting active erosion of the canyon floor by mudclast-rich flows. (G) Sandstone injectite in a mudstone block within a debrite.

with a tendency towards the south-east, with common opposing directions (Fig. 7J). Bioturbation intensity is variable but generally high.

Interpretation: This thin-bedded and fine-grained facies association was deposited outside channel-scale confinement, but within the canyon confinement, supporting an interpretation of a confined overbank setting. The finer-grained, more dilute parts of turbidity currents are either flow stripped, or overspilled, from the axis to deposit thin-bedded turbidites. The more concentrated part of rare larger magnitude flows deposit the thicker bedded and coarser-grained turbidites. Medium-bedded sandstone with dune-scale cross-bedding (Fig. 7F) implies outsized flows that deposited and tractionally reworked sand on the overbank (e.g. McArthur *et al.*, 2020). The pebble lags (Fig. 7A) within thin-bedded turbidite successions also support rare high-energy flows that transported, winnowed and bypassed sediment in this setting (Allen *et al.*, 2022). The flat-topped coarse-grained lenses (Fig. 7G) also indicate overspill of high-energy axial flows that develop high aspect ratio (*ca* centimetres thick, metres wide) 'secondary channels' (e.g. Hein & Walker, 1991). Starved ripple lamination (Fig. 7I) and laminae (Taylor *et al.*, 2024a) indicate that overbanking flows were occasionally sediment-starved. Complex facies distributions, scour surfaces (Fig. 7H) and palaeocurrent patterns point to flow interaction with the canyon wall or depositional and erosional relief in the overbank driving reflection and deflection (Kane *et al.*, 2010; Taylor *et al.*, 2024b). High-amplitude ripples with mud-rich troughs and low amplitude ripples with varying mud content are interpreted as a mixed-grain size bedform related to unidirectional transitional flows that developed through entrainment of cohesive mud (Taylor *et al.*, 2024a). The influence of internal tides reworking the confined overbank cannot be ruled out (Taylor *et al.*, 2024b).

Shallow marine canyon-fill deposits
Description: This facies association (up to 15 m thick) is dominated by thick-bedded sandstones and minor heterolithic deposits (up to tens of centimetres thick). The base surface truncates channel margin or overbank deposits. The top of this facies association is marked by the El Gallo Formation unconformity. Sandstone beds are dominantly low-angle cross-laminated (Sl; Fig. 5F) and commonly grade into sandstones with symmetrical ripple lamination (Sw; Fig. 5G) and thinly interbedded sandstones and mudstones (H). Siderite concretions and siderite-cemented *Ophiomorpha* and *Thalassinoides* burrows are common. Mudclast breccias (Dm; Table 1; Fig. 5I) are found in the thickest beds. Upward thinning trends are common. In one instance this is preceded by an upward thickening trend. Palynofacies consist of mixed opaques and Amorphous Organic Matter with poor recovery and poor preservation, and deposits are rich in *Gonylacoid* dinoflagellate cysts (see Supporting Information).

Interpretation: This facies association is interpreted to represent shallow marine conditions. Low-angle cross-lamination in combination with symmetrical ripples and siderite cement is typical of near-shore depositional environments (Reading, 1996). The upward thickening-then-thinning trends likely represent shoreface advance and retreat. The ichnofacies and palynofacies support a more restricted environment compared to the deep-water deposits in the rest of the canyon fill. The detrital-zircon-derived age and stratigraphic position of this facies association below the El Gallo Formation unconformity leads the authors to conclude that these are transgressive deposits, preserved below the main ravinement surface of the El Gallo Formation, in the embayment that the Punta Baja canyon head likely formed at that time.

A

Differential compaction

10cm

Gravel lag in thin-bedded turbidites

B

Bypass surface

Disconnected loadballs

10cm

C

Ejected mud-clasts

Dewatering

D

5cm

Steep climbing ripple lamination

Low angle climbing ripple lamination sets

E

Low-angle cross-bedding

10cm

F

10cm

Coarse sand bedform

Overbank thin beds above and below

G

Crevasse deposits?

Very coarse sand - gravel

Overbank thin beds above and below

Compensational stacking

10cm

I

Starved ripples

10cm

H

Shallow scour surfaces

Scour with dune-like cross-bedding fill
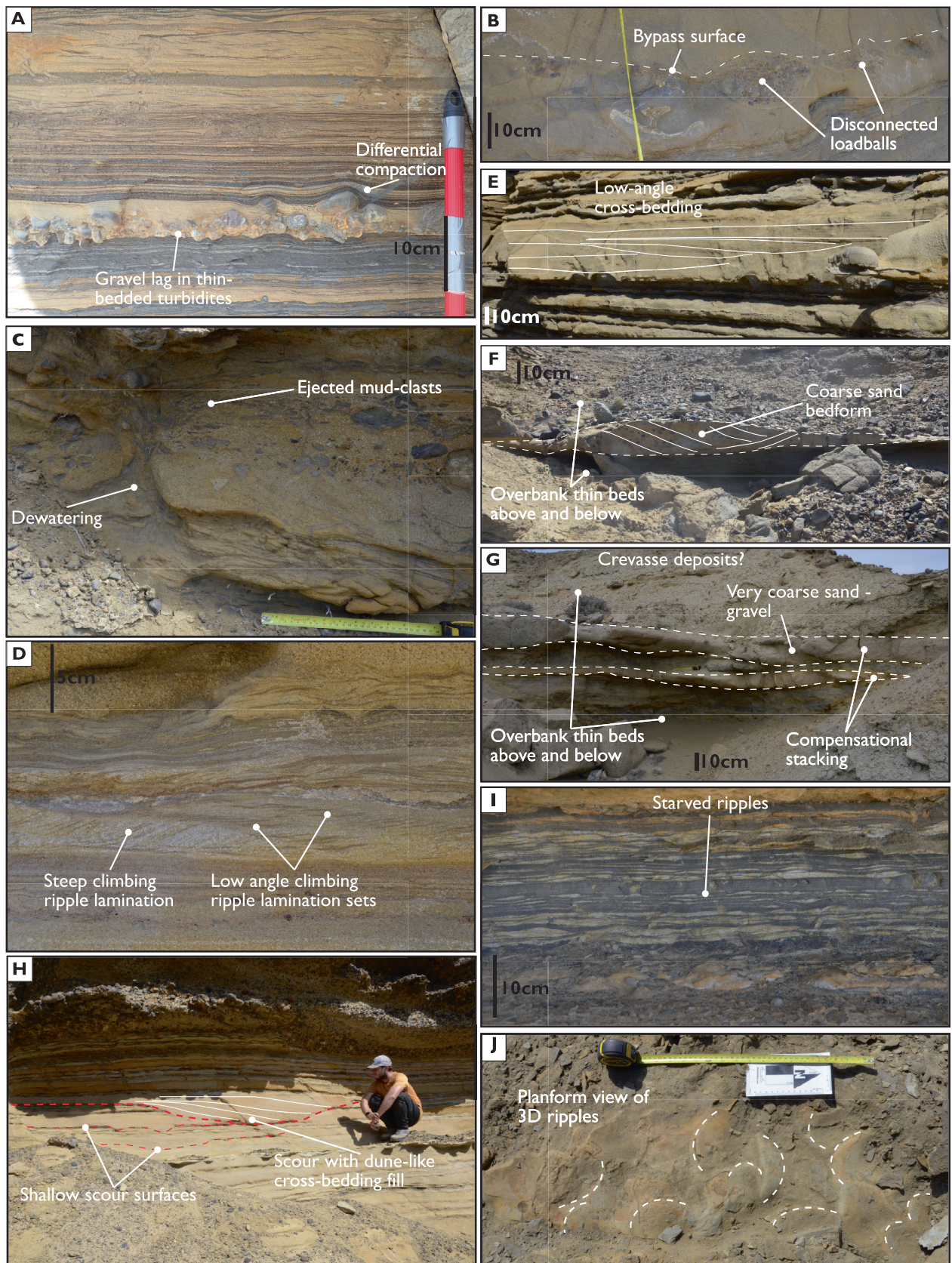
J

Planform view of 3D ripples

Fig. 7. Representative field photographs of depositional and erosional bedforms in generally fine-grained deposits. (A) Gravel lag in thin-bedded turbidites, suggesting high-energy flows in an otherwise low-energy depositional environment. Overlying beds are deformed due to differential compaction around protruding clasts. (B) Disconnected conglomeratic loadballs in sandstones, indicating sediment bypass on the truncating surface. (C) Dewatering pipe in sandstones with mudclast-rich intervals above. (D) Steep climbing ripple lamination and low-angle climbing ripple lamination. (E) Low-angle cross-bedded sandstone indicating flow interaction with topography. (F) Outsized sandstone bed in thin-bedded canyon overbank deposits, showing dune-scale cross-bedding and hummock-like cross-bedding. (G) Sandstone beds with variable thickness within thin-bedded canyon overbank deposits, showing subtle compensational thickness relations. These could represent crevasse deposits on the canyon overbank. (H) Shallow scour surfaces in channel margin sandstone deposits, some infilled with dune-like cross-bedded sandstones with a height equal to the depth of the scour. This indicates that the cross-bedding did not directly result from a migrating bedform but instead represents the gradual infill of a depression. (I) Starved ripple lamination in heterolithic deposits. (J) Variable crescentic ripple crest orientation in plan view.

Canyon-fill architecture

The Punta Baja canyon-fill forms a 5 × 2 km exposure, mainly as coastal cliffs, with a general south-west palaeocurrent direction (Fig. 4). It is incised into the fluvial bedrock of the Bocana Roja Formation (Fig. 10A and B). This contact is exposed in multiple places around the peninsula.

One dip and three strike cross-sections were constructed by projecting field mapping and measured sections on DEM-derived topographic profiles, assisted by virtual outcrop models. The chosen strike sections provide different stratigraphic windows into the canyon fill succession with X3 stratigraphically the lowest and X1 the highest (Fig. 9).

Canyon wall

Observations: The steep erosional contact between the Bocana Roja Formation subcrop and the Punta Baja Formation canyon-fill is well-exposed along the eastern and western sides of the peninsula (Fig. 10). The canyon wall erosion surface in the east truncates fluvial floodplain deposits and braided stream conglomerates of the Bocana Roja Formation (Fig. 10A and B), and is overlain by mud-rich mass transport and overbank heterolithic deposits of the canyon fill (Figs 9 and 10C). The western canyon wall truncates floodplain deposits of the Bocana Roja Formation and is dominantly overlain by axial canyon-fill conglomerates (Fig. 10D to F). Locally, the canyon wall is scalloped and overlain by chaotic facies. (Fig. 10). In the west, these scallop surfaces are filled with dark pebbly mudstone and thin-bedded turbidites steeply onlapping the contact (Fig. 10E). In the east, a conglomeratic and coarse sand-filled scallop overlies the canyon wall, in an otherwise thin-bedded depositional environment.

Overall, the eastern margin is dominantly overlain by channel margin and overbank deposits, and the western margin by axial conglomerates. A notable exception is on the western side of the peninsula, where a 10 m thick interval with a wide variety of facies is found overlying the canyon wall (Fig. 11).

Interpretation: The range of smaller-scale erosional features on the canyon wall are interpreted as representing slide scars, chutes and gullies that shaped the canyon margin. The common occurrence of chaotic facies above the erosional base of the canyon wall is inferred to represent continual erosion and degradation of the canyon walls during filling. The resulting irregular canyon wall relief would have formed terrace surfaces of different heights and shapes providing the topography to result in a range of facies onlapping the canyon wall.

Lower fill

Observations: The lowermost exposed canyon fill is dominated by unorganized and poorly sorted conglomerates containing large (*ca* 4 m diameter) angular clasts of red sandstone from the Bocana Roja Formation bedrock (Fig. 12A and B). Within these chaotic conglomerates sit sand-prone scour-fills and channel-fills with complex cross-cutting relationships and pebble-lined bypass surfaces (Fig. 12C and D).

Interpretation: The dominance of unorganized conglomerates and large clasts signifies ongoing canyon wall excavation during canyon fill. The more organized scour and channel fill deposits are interpreted as braid-plain deposits that accumulated during the initial high-energy filling of the canyon (Fig. 12A).
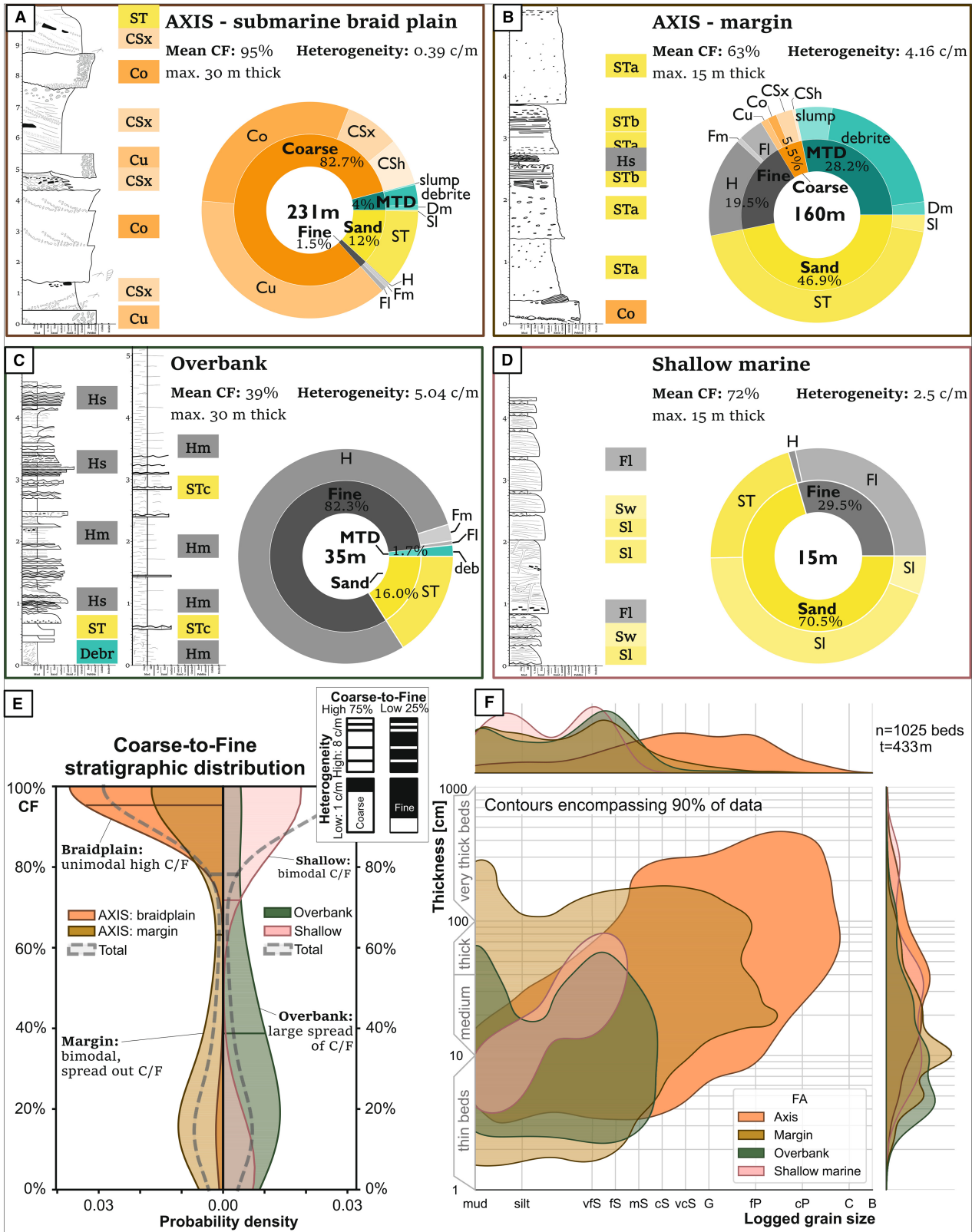
Fig. 8. Overview, characteristics and facies statistics of facies associations: canyon axis braid plain (A); canyon axis margin (B); canyon overbank (C); and shallow marine (D). Representative measured sections of each facies association are labelled with facies (Table 1). Doughnut plots of facies make-up in percentage of total stratigraphic thickness per facies association, categorized by mean grain size being in the mud, sand or coarser range. Mean CF represents the percentage of stratigraphy with a logged grain size coarser than silt. Heterogeneity (in changes per metre or c/m) indicates how the coarse versus fine lithologies are distributed; high heterogeneity means that coarse and fine lithologies are interspersed, while low heterogeneity implies a more clustered distribution and thicker intervals of the same class, see also inset in (E) coarse to fine distribution per bed per facies association, on a probability density scale, which gives more detail than the mean value. (F) Logged grain size versus bed thickness of beds in each facies association.

Upper fill

Observations: Braid-plain deposits in the eastern part of the canyon fill are overlain by, and laterally interfinger with, mud-rich debrites with blocks of contorted thin bedded turbidites (Fig. 9, for more detail see Supporting Information). The conglomerates at the base are steeply truncated towards the west. The north–south oriented truncation surface is overlain by deformed turbidites and rotationally slumped thick-bedded channel margin deposits. The failure direction as indicated by slump vergence is to the west, perpendicular to the truncation surface (Fig. 9, for more detail see Supporting Information). These slumps are onlapped by axial deposits towards the west. Multiple erosional surfaces inclined towards the west are overlain by organized conglomerates (Fig. 13).

Finer-grained and heterolithic deposits are preserved mainly on the eastern canyon margin, and thin and fine upward. In contrast, conglomeratic deposits stack vertically and amalgamate along the western canyon margin. A thick (<10 m) interval of medium to thick-bedded sandstones and thinner-bedded heterolithic deposits is preserved along the western side of the field area, bounded by conglomeratic deposits below and above. West to south-west-oriented conglomerate-filled scour surfaces truncate these thick-bedded sandstone channel margin deposits (Fig. 6E), and in most places amalgamate with underlying conglomeratic braid-plain deposits.

Interpretation: The preservation of multiple erosional surfaces overlain by organized conglomerates suggest that these are cut-bank surfaces overlain by channel-fills; a westward migration of the channel belt is suggested by the preservation of multiple cutbank surfaces and fills (Fig. 13). This geometry and process interpretation is akin to the 'lateral step remnants' proposed by Kane *et al.* (2010), to differentiate such deposits from lateral accretion, which has

also been recognized in seismic reflection datasets but attributed to channel avulsion (Abreu *et al.*, 2003). The eastward fining from conglomerates, which are stacked and amalgamated, to thick-bedded sandstones, to thin-bedded heterolithic deposits, suggest a transition from channel axis, to channel margin, to overbank (Taylor *et al.*, 2024b).

Mass-transport deposits

Observations: In the northernmost upstream part of the field area, the sand-rich channel margin deposits are overlain by, and interbedded with, mud-rich debrites and slumped deposits (Fig. 14A). Sandstone lenses intercalated with the debrites and slumps display erosive to conformable bases with multi-directional fanning geometries (Fig. 14D), and a general thinning-upward and fining-upward trend. Palaeocurrents from ripples and low-angle cross-bedding show a wide dispersal direction (Fig. 14C). *Tisoa* burrows are locally abundant below erosion surfaces.

Interpretation: This succession is interpreted to represent multiple mass-wasting events with sandstones foundering above, and channels navigating across, mass transport relief. Their mud-rich or thin-bedded composition suggests a source from the submarine deposits accumulating on the unstable canyon wall. The sandstones containing complex palaeoflow indicators suggest flow reflection and deflection from mass transport and canyon wall topography. The *Tisoa* burrows below erosion surfaces suggest that conduits were active and open above these mass-transport deposits (Knaust, 2019), and can be used to interpret periods of sediment bypass (Stevenson *et al.*, 2015).

Up-flow dipping surfaces

Observations: Generally, sedimentary surfaces within the axial conglomerates of the Punta Baja canyon-fill are steeper (>5°) than the regional
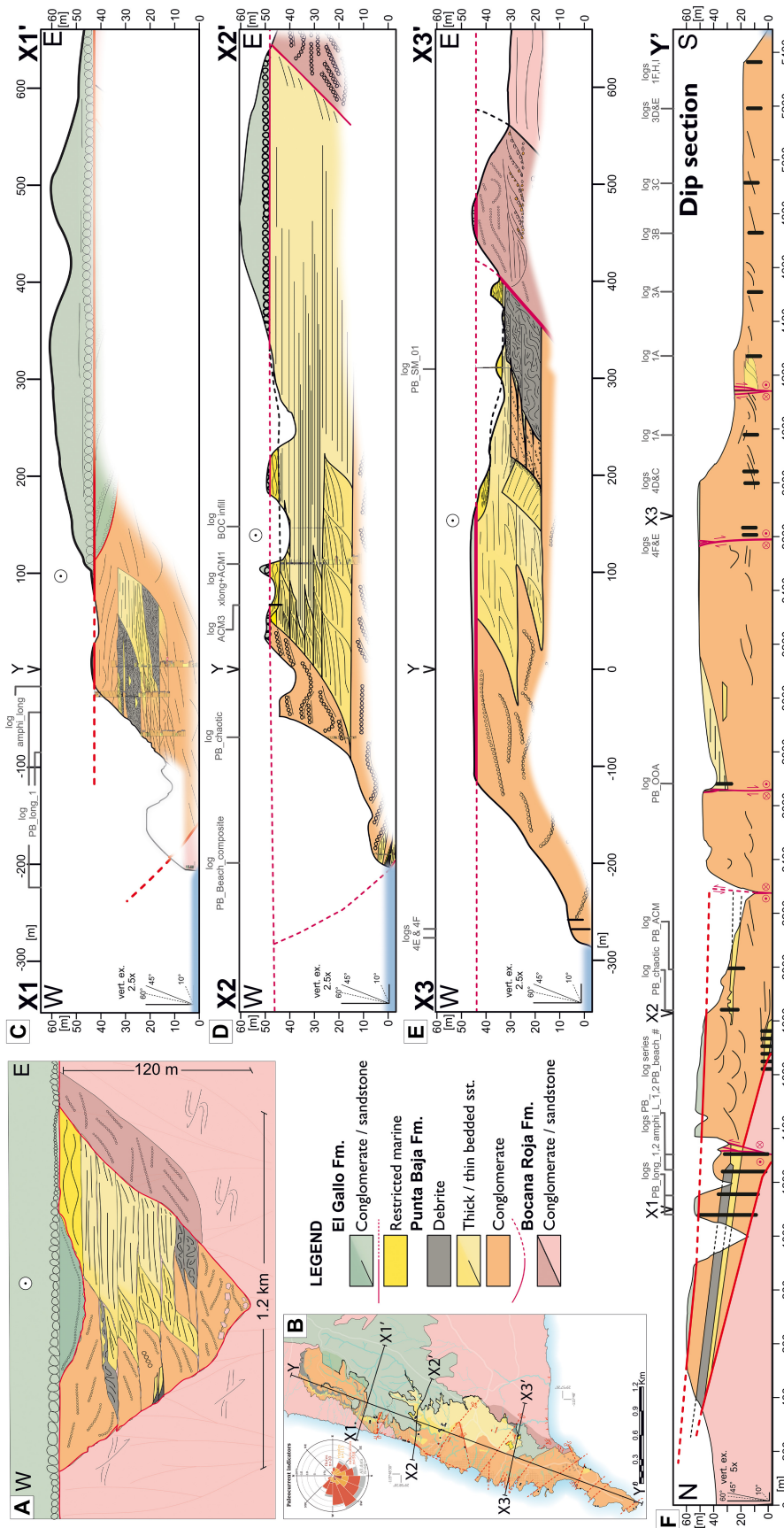
Fig. 9. (A) Composite schematic strike cross-section of exposed canyon fill. (B) Map and palaeocurrent rose diagram of Fig. 4 with location of cross-sections in (C) to (F) indicated. (C) to (F) Strike and dip panels with projected mapped facies boundaries, logged sections and Uncrewed Aerial Vehicle (UAV)-assisted orientation of surfaces. Note the vertical exaggeration in each panel by slope diagram in the lower left of each panel. Due to regional tectonic deformation, the strike-oriented panels (C) to (E) provide windows into different stratigraphic levels; panel X3 (E) covers the lowest stratigraphy, panel X1 (C) the highest stratigraphy of the exposed canyon fill.

tectonic tilt (2° to 5°) of bedding surfaces. Due to the extensive dip-exposure of axial canyon deposits in the field area, the spatial extent and 3D orientation of metre to tens of metres scale sedimentary dip surfaces in coarse-grained canyon fills is documented for the first time in outcrop. Small-scale scours form complicated three-dimensional surfaces. Therefore, only larger-scale planar surfaces are included in the analysis, and concave erosional scours and convex dune-scale bedforms are excluded. The scale of the measured surfaces exceeds the bed scale with a mean measured plane length of 10.2 m, and a mean dip of 12.7°. Most surfaces (68%) are upstream-inclined, with a mean dip direction to the ENE. This is nearly opposite to the mean south-westward flow direction from conglomerate clast imbrication (Fig. 15C).

Note that the apparent even distribution of dip directions in Fig. 15D is optical. To test whether the visual directional trend from the Rose diagram bears statistical significance, three uniformity tests were carried out (Baas, 2000). The Kuiper test yielded a test parameter V_n of 0.2079, above the threshold $V_{\alpha=1\%}$ of 0.0863 and thereby indicating a directional character of the data at a confidence level of 99%. The Watson test failed the 99% confidence threshold $u^2_{\alpha=1\%}$ of 0.267, but with a test parameter u^2 of 0.248 cleared the 95% confidence threshold $W_{\alpha=5\%}$ of 0.187 indicating directional data. The Rayleigh test yielded a test parameter R of 0.2927, surpassing the $R_{\alpha=1\%}$ critical value of 0.0943 indicating directional data at 99% confidence.

The pervasive upstream orientation of sedimentary surfaces is not caused by post-depositional tectonic tilting, since 76.7% of the mapped sedimentary surfaces dip more steeply (between 5° and 30°; Fig. 15D) than the structural tilt (<5° SSW) of the Punta Baja Formation. Moreover, the structural tilt is south-westward (Fig. 15A and B) in the same direction as regional palaeoflow, which should cause over-representation of apparent downstream dipping surfaces.

Interpretation: The steepness of these surfaces, whether resulting from erosion or deposition, was maintained because conglomerates have a higher angle of repose and stability of the seabed compared to their sand-rich equivalents. Upstream dipping surfaces clearly dominate over downstream, and flow-perpendicular orientations show a tendency to the south-east. This variability is probably caused by local variations in axis thalweg direction, sinuous braid-plain

channel planforms and outcrop orientation. Based on palaeoflow orientation with respect to these large-scale surfaces these features are interpreted as backsets developed on supercritical bedforms, such as cyclic steps.

El Gallo unconformity
Observation: The nature of the Punta Baja Formation contact with the overlying El Gallo Formation is variable, consisting of an undulating surface overlain by yellow-weathering shallow marine deposits and/or a layer of very well-rounded bored-boulders within a white fine-grained matrix (Fig. 16A), which locally is preceded by red-weathering matrix-supported gravels with angular clasts (Fig. 16B). The age of these shallow marine deposits, as indicated by detrital zircon dating (78.5 ± 0.9 Ma), is younger than other canyon-fill deposits (minimum 80.8 ± 1.0 Ma), but also older than El Gallo Formation (maximum 72.3 ± 0.5 Ma) samples in the area (Fig. 9; Supporting Information).

Interpretation: This surface is interpreted as an erosional unconformity, associated with sea-level fall and erosion, ravinement and deposition of a boulder beach deposit during transgression. Micropalaeontological samples suggest an open, but relatively restricted, marine setting (see Supporting Information) for the overlying El Gallo Formation.

DISCUSSION

Canyon evolution

Incision to fill
Structural data demonstrates that the Punta Baja canyon-fill is aligned with fault patterns in the canyon subcrop, the Bocana Roja Formation, which formed through syn-depositional and post-depositional contractional and extensional deformation in response to dextral strike-slip movement (Fig. 4), in agreement with Kane *et al.* (2022). A local tectonic stress regime superimposed on regional subsidence may have formed a relatively minor structural depression that was enough to divert submarine sediment gravity flows from the regional west-dipping slope (Fig. 17, t1). Initial capture and focussing of sediment gravity flows enhanced erosion of the bedrock and promoted incision and deepening of the nascent canyon (Fig. 17, t2). Scallop-shaped erosion surfaces on the canyon wall overlain by chaotic facies representing slide
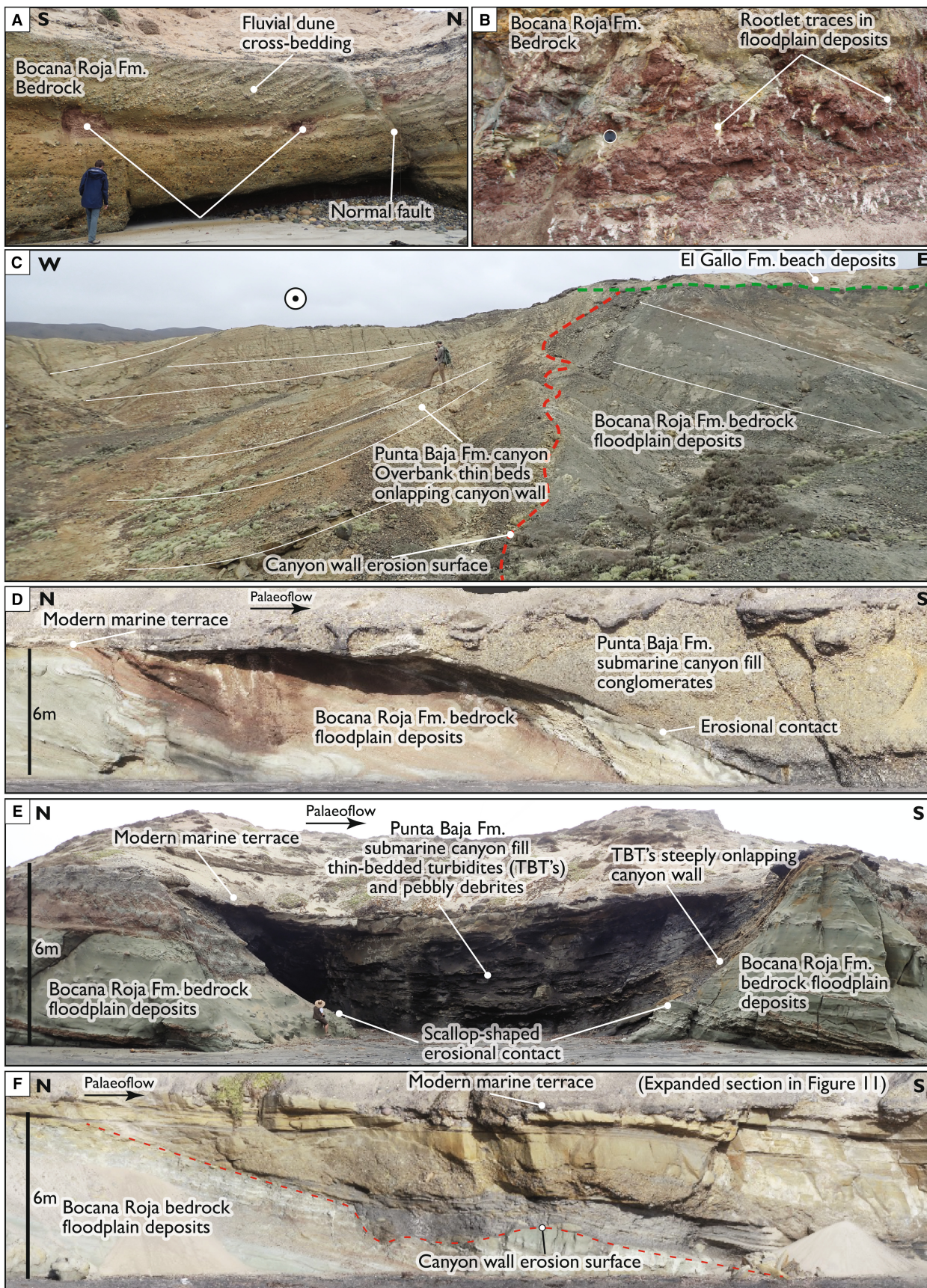
A S — Fluvial dune cross-bedding — N — Bocana Roja Fm. Bedrock — Normal fault

B Bocana Roja Fm. Bedrock — Rootlet traces in floodplain deposits

C W — El Gallo Fm. beach deposits — E — Punta Baja Fm. canyon Overbank thin beds onlapping canyon wall — Bocana Roja Fm. bedrock floodplain deposits — Canyon wall erosion surface

D N — Palaeoflow — S — Modern marine terrace — Punta Baja Fm. submarine canyon fill conglomerates — 6m — Bocana Roja Fm. bedrock floodplain deposits — Erosional contact

E N — Palaeoflow — S — Modern marine terrace — Punta Baja Fm. submarine canyon fill thin-bedded turbidites (TBT's) and pebbly debrites — TBT's steeply onlapping canyon wall — 6m — Bocana Roja Fm. bedrock floodplain deposits — Bocana Roja Fm. bedrock floodplain deposits — Scallop-shaped erosional contact

F N — Palaeoflow — Modern marine terrace — (Expanded section in Figure 11) — S — 6m — Bocana Roja bedrock floodplain deposits — Canyon wall erosion surface

Fig. 10. Field photographs and two-dimensional captures from photogrammetric-models of the variable nature of the canyon fill erosional contact with the underlying Bocana Roja Formation. (A) Steep dune-scale cross-bedded conglomerates representing alluvial braided stream deposits of the Bocana Roja Formation on the eastern side of the canyon fill erosion surface. Person for scale is *ca* 1.8 m tall. (B) Finer-grained floodplain deposits of the Bocana Roja Formation to the west and further east of the canyon fill erosion surface (see lens cap, 55 mm in diameter, for scale). (C) Eastern canyon wall contact between Bocana Roja Formation floodplain deposits and onlapping Punta Baja Formation submarine canyon fill thin-bedded overbank turbidites. Palaeoflow is out of the page. (D) Western canyon wall contact between Bocana Roja Formation floodplain deposits and Punta Baja Formation submarine canyon fill conglomerates. (E) Western canyon wall scalloped contact between Bocana Roja Formation floodplain deposits and Punta Baja Formation submarine thin-bedded turbidites and dark mud pebbly debrites, representing a chute or gully on the canyon wall and inferring major bypass. (F) Western canyon wall contact between Bocana Roja Formation floodplain deposits and a variety of Punta Baja Formation submarine facies (more detail in Fig. 10).

scars, chutes and gullies coincide with subcrop faults. A sand-rich canyon wall gully-fill on the eastern canyon margin suggests that smaller lateral conduits transferred sediment into the canyon, in this case depositing outsized sediment in the overbank environment. The lowermost canyon fill, comprising chaotic conglomeratic deposits with abundant clasts from the adjacent bedrock (Fig. 12), represent coarse-grained lag deposits and a sediment bypass-dominated period (Dailly, 1982; Normark *et al.*, 1993; Stevenson *et al.*, 2015). Overall, this phase of canyon formation was dominated by erosion, sediment bypass and canyon wall failure.

Early fill
During the incisional phase, dilute parts of bypassing turbidity currents ran up the canyon wall to deposit fine-grained thin-bedded turbidites above the irregular topography of the canyon margins (Fig. 10E). Accumulations of thin-bedded turbidites were remobilized to form mud-rich mass-transport deposits in the Punta Baja canyon-fill. Lateral canyon wall failure caused instantaneous widening of confinement, allowing passing flows to expand and become depositional. The mass-transport deposits formed topographic barriers to flows (Fig. 17, t3). Multiple phases of mass-transport deposition and canyon floor aggradation could have been entirely eroded while the highly energetic canyon was deepening. However, the combination of instantaneous canyon widening and decreased thalweg gradient due to mass-transport deposition, promoted the (local) onset of canyon floor aggradation.

Aggradational fill
The oldest preserved confined overbank deposits on the eastern margin mark the aggradational stage of the canyon fill. As the canyon filled and the floor became elevated, and thus wider, flows focussed in an axial thalweg were stripped and overspilled onto the overbank. Erosional entrenchment of the thalweg could have forced lateral flow segregation due to the elevation difference between the lower high-concentration and upper low-concentration parts of stratified flows. Mass-transport deposits also formed superelevated relief above the thalweg. Thus, flow stripping and overspill from the thalweg confinement aggraded local overbank successions. The emplacement and preservation of mass-transport deposits coincides with the onset of overbank accumulation (Fig. 17, t4).

Axial thalweg migration is recorded by westward-cutting-and-aggrading channel margin deposits, grading eastward and upward into thin-bedded overbank deposits (Fig. 13). The canyon-fill asymmetry suggests that, overall, the axis migrated westward, contributing to the upward fining and thinning trend on the eastern overbank area. This asymmetry may be attributed to tectonic releasing bend characteristics, with the centre of active extensional tectonism stepping north and westward through time (Kane *et al.*, 2022). Additional contributing factors for the architectural asymmetry could have been the regional westward sloping and tilting basin margin and the pinning of a channel outer bend (Brunt *et al.*, 2013). Rotational slumping of eastern channel margin deposits (Fig. 9, X3) supports the interpretation that active incision was focussed on the western margin of the canyon.

Thalweg widening followed by entrenchment, and pulses of eastward thalweg migration, and/or bank erosion, resulted in remnants of lateral steps on the eastern side of the thalweg (Fig. 13), when axis migration resumed its general westward
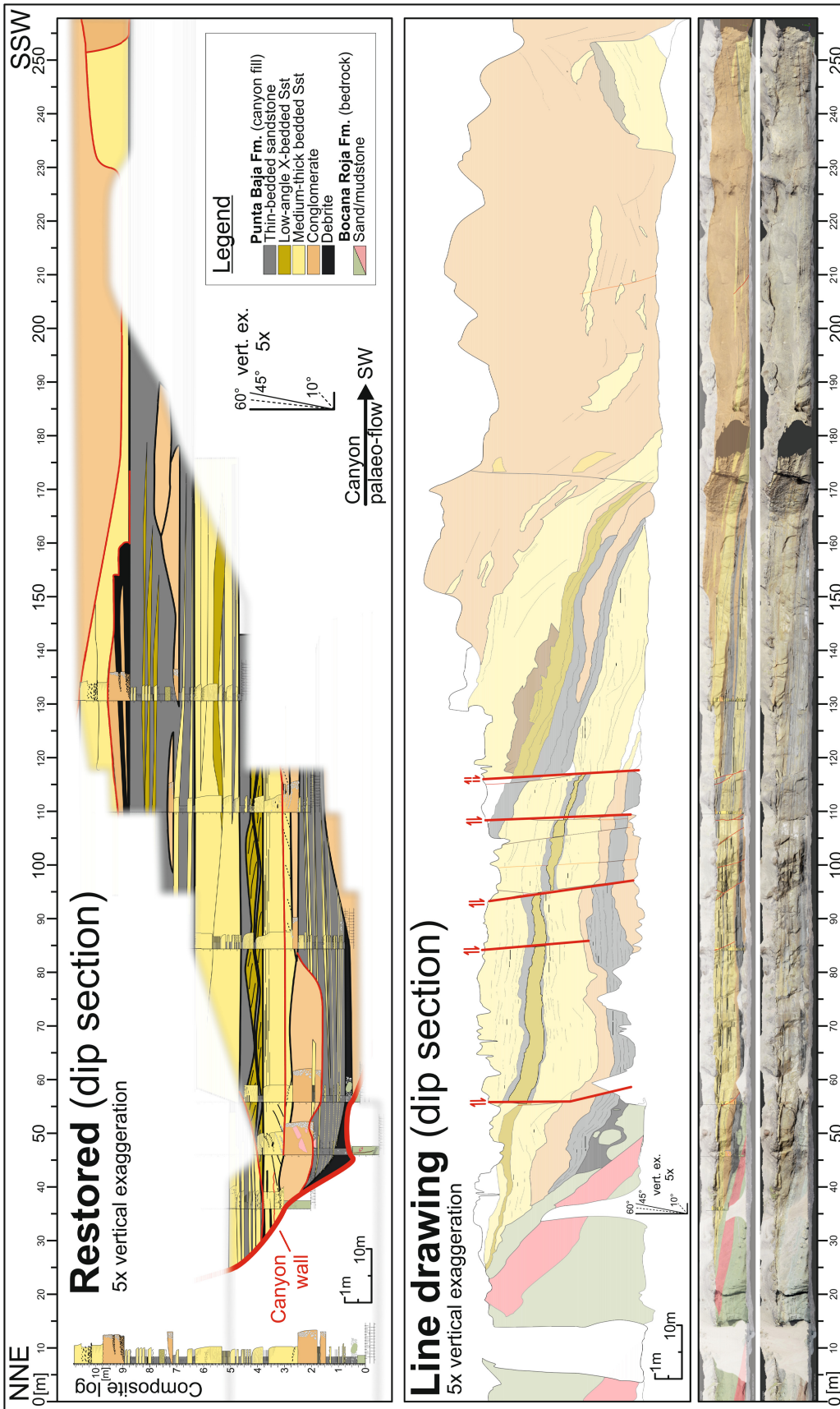
Fig. 11. Capture from a three-dimensional virtual outcrop model of a more than 250 m long dip exposure of canyon bedrock (Bocana Roja Formation), incision surface and submarine canyon fill (Punta Baja Formation), with interpreted facies relations and depositional geometries (lowermost subfigure). The line drawing is vertically exaggerated in the middle subfigure and restored for post-depositional faulting in the uppermost subfigure. The panel shows that the canyon wall is overlain by a wide variety of canyon fill facies: mud-rich debrites, thin-bedded turbidites, conglomeratic channel fills, low-angle cross-bedded sandstones that are interpreted to represent flow reflection off the canyon wall. These facies juxtapositions indicate that a variety of flow types and magnitudes interacted with the canyon-bounding surface, and these variable properties led to complex depositional patterns.
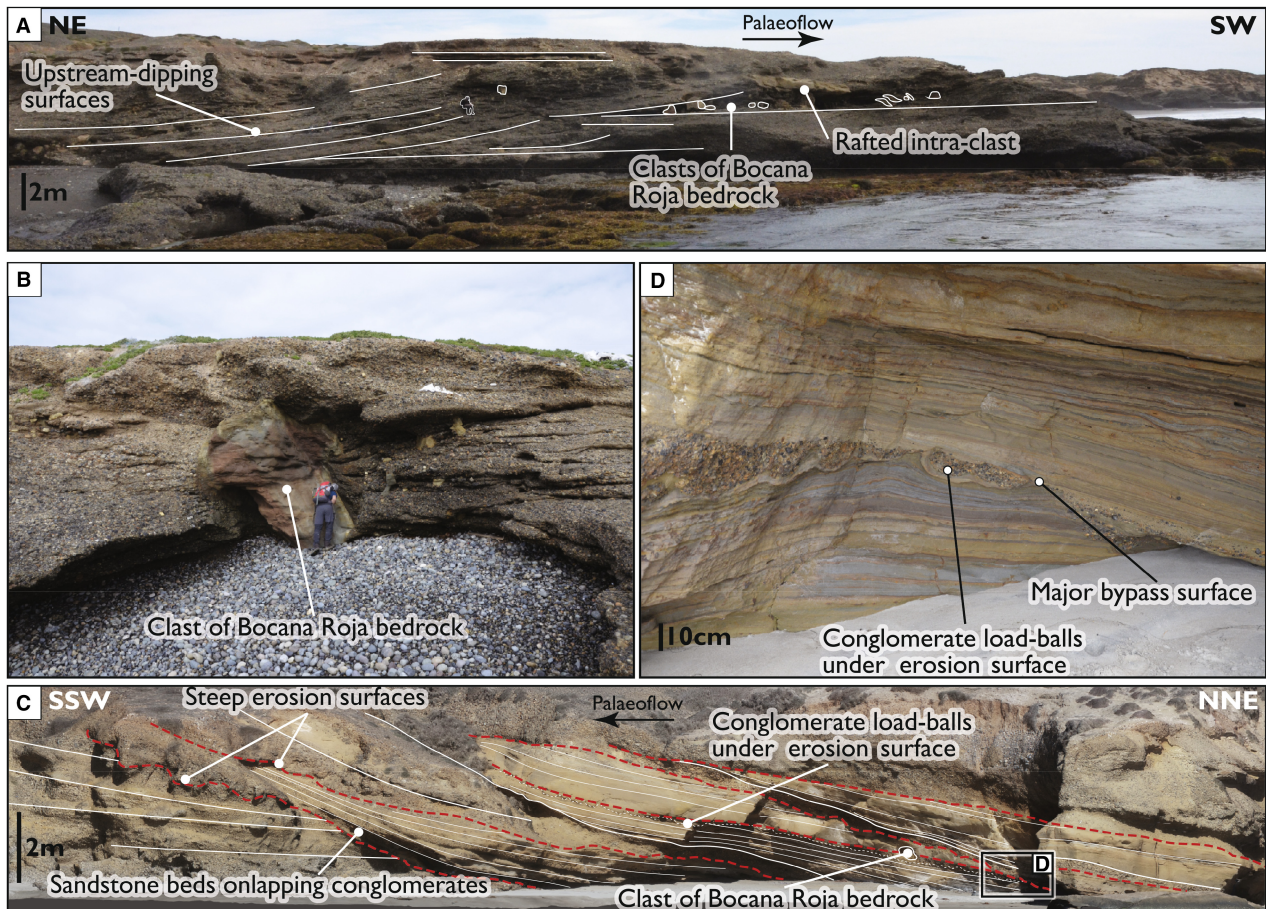
Fig. 12. Characteristics of the lower canyon fill. (A) Amalgamated conglomeratic deposits with clasts of Bocana Roja bedrock and a rafted intraformational clast, showing common up-stream dipping surfaces. (B) A large clast (4 m diameter) of Bocana Roja bedrock with original bedding preserved, within Punta Baja canyon fill conglomerates. (C) Steep erosion surfaces overlain by conglomerate and onlapped by medium to thin-bedded turbidites. Erosion surfaces stepping up-stream, possibly representing migrating channels on the submarine braid plain, filled with sand-rich turbidites. (D) Detail of (C) showing conglomerate load-balls within thin-bedded turbidites, sometimes completely removed and the only evidence of high-energy deposits that were since removed, and thus representing a major bypass surface.

tendency (Fig. 17, t4). The repeated bank cutting, and gradual accretion of the channel margin and overbank suggests that the canyon was an active conduit for flows that transported and largely bypassed a wide range of grain sizes during filling.

The thick accumulation of channel margin deposits can represent: (i) a westward migration of the canyon axis, with laterally equivalent braid-plain deposits now eroded beyond the western coastline; or (ii) a decrease in grain size delivered to these reaches of the canyon, resulting in sand-rich channel systems filling the canyon thalweg. The latter could be caused by an upstream intra-canyon blockage trapping the gravel fraction, a relative sea-level rise after which the sediment delivery had to re-adjust, or a change in sediment supply from the hinterland drainage system. The presence of gravel lags in the channel margin deposits supports a more western axis with its conglomeratic braid-plain deposits unexposed.

Continued erosion caused canyon wall failure and the emplacement of a thick succession of mass-transport deposits in the canyon axis. Flows were diverted or partially blocked by the positive relief of these mass-transport complexes (Fig. 17, t5). When gravity flows eventually overcame the depositional relief, the canyon thalweg re-established in a more eastward (canyon-central) position, incising into the mass-transport deposit and underlying channel margin deposits.
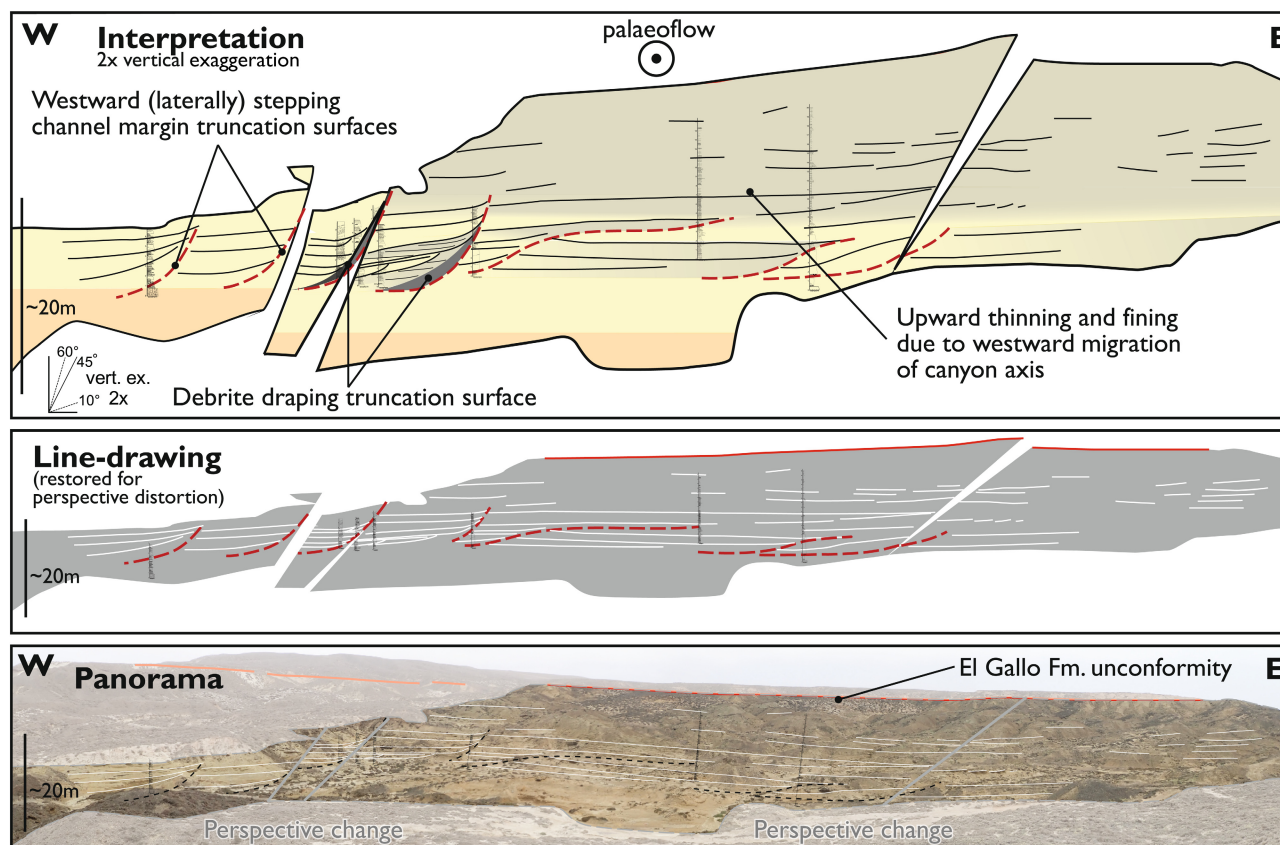
Fig. 13. Photographic panel and reconstructed interpretation of westward laterally stepping channel margin deposits. The vertical fining facies succession and westward stepping of erosion surfaces reflect a westward migration of the canyon axis, resulting in decreasing energy levels in its eastern parts. Multiple erosion surfaces are overlain by muddy debrites, reflecting the bank failure and erosion upstream of this location.

This net-aggradational phase of canyon development shows evidence of a highly efficient conduit, that eroded and bypassed sediment in an entrenched axis, while an overbank aggraded. The conglomeratic axial fill with sandstone-filled scours suggests that flows bypassed grain sizes up to pebble/cobble through the axis, with the higher, sand-bearing and mud-bearing parts of flows partially stripping and spilling onto the overbank. The abundant erosional structures, coarse-grained lags and down-canyon palaeocurrent directions in the overbank deposits suggest that even bank-overspilling flows underwent a high degree of down-canyon bypass.

Late fill

No stratigraphic evidence remains for further stages of canyon evolution, owing to the El Gallo Formation ravinement unconformity. However, the more restricted or shallow marine character of the early El Gallo Formation deposits suggests deposition in a shelf-incised embayment, possibly prior to the complete infill of the canyon head.

Controls on submarine canyon-fill sedimentology and stratigraphy

Interaction of sediment gravity flows with mass-transport topography

Mass-transport deposits in the Punta Baja canyon fill are common and are shown to impact canyon sedimentation and erosion patterns profoundly, as has been recognized in seismic reflection data (e.g. Gong *et al.*, 2011; Wang *et al.*, 2017; Liang *et al.*, 2020), outcrop investigations (Allen *et al.*, 2022) and modern canyon observations (Pope *et al.*, 2022). The restoration of channel gradients across mass-transport deposits has at least partially been attributed to upstream migrating knickpoints or knickpoint zones (Tek *et al.*, 2021; Allen *et al.*, 2022). The increased gradient on the
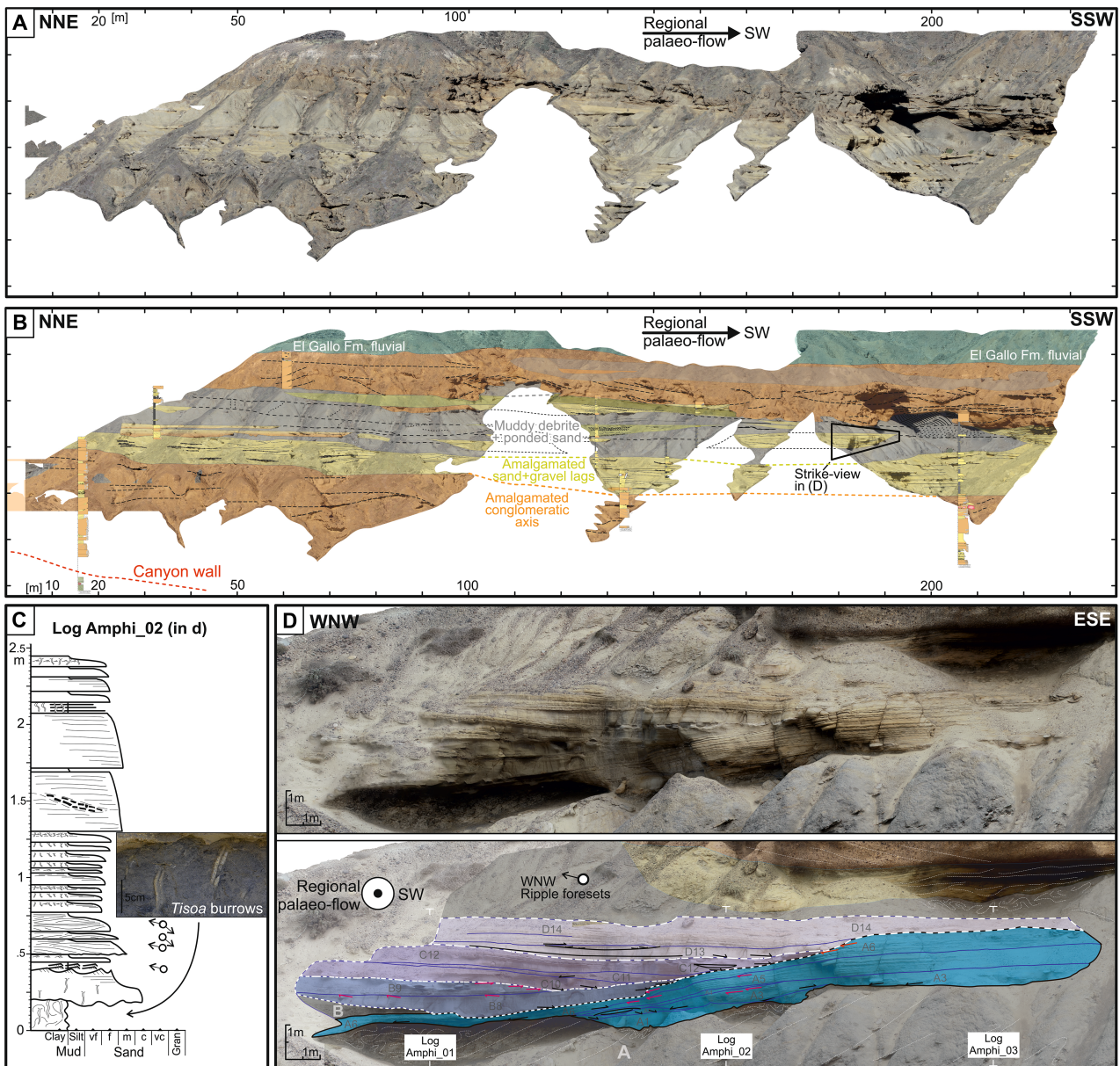
Fig. 14. (A) Three-dimensional outcrop model orthographic render of northern cliff dip-section. (B) Interpretation highlighting depositional environments and measured sections. (C) Example sedimentary log through a ponded sandstone body within the mass-transport complex. The *Tisoa* burrows suggest that the erosion surfaces were sustained open sediment conduits before filling. (D) Strike view of a sandstone body within the mass-transport complex, interpreted as several phases of sand deposition over a partly mobile substrate, causing complex dip orientations and cross-cutting relationships.

downstream part of the mass-transport deposits is likely to induce knickpoints, which incise headward across the mass-transport deposit and produce steep, stepped and composite erosion surfaces (Allen *et al.*, 2022). These may be infilled with coarse-grained and fining-up terrace deposits, or channelized sandstones. Foundering

sandstone deposits on the mass-transport complex relief (Fig. 14) indicate that sand-bearing parts of flows surmounted the mass transport relief (e.g. Martínez-Doñate *et al.*, 2021). Pebbles and cobbles were likely transiently stored upstream of the mass-transport complex relief, as is observed in the modern Congo Canyon (Pope
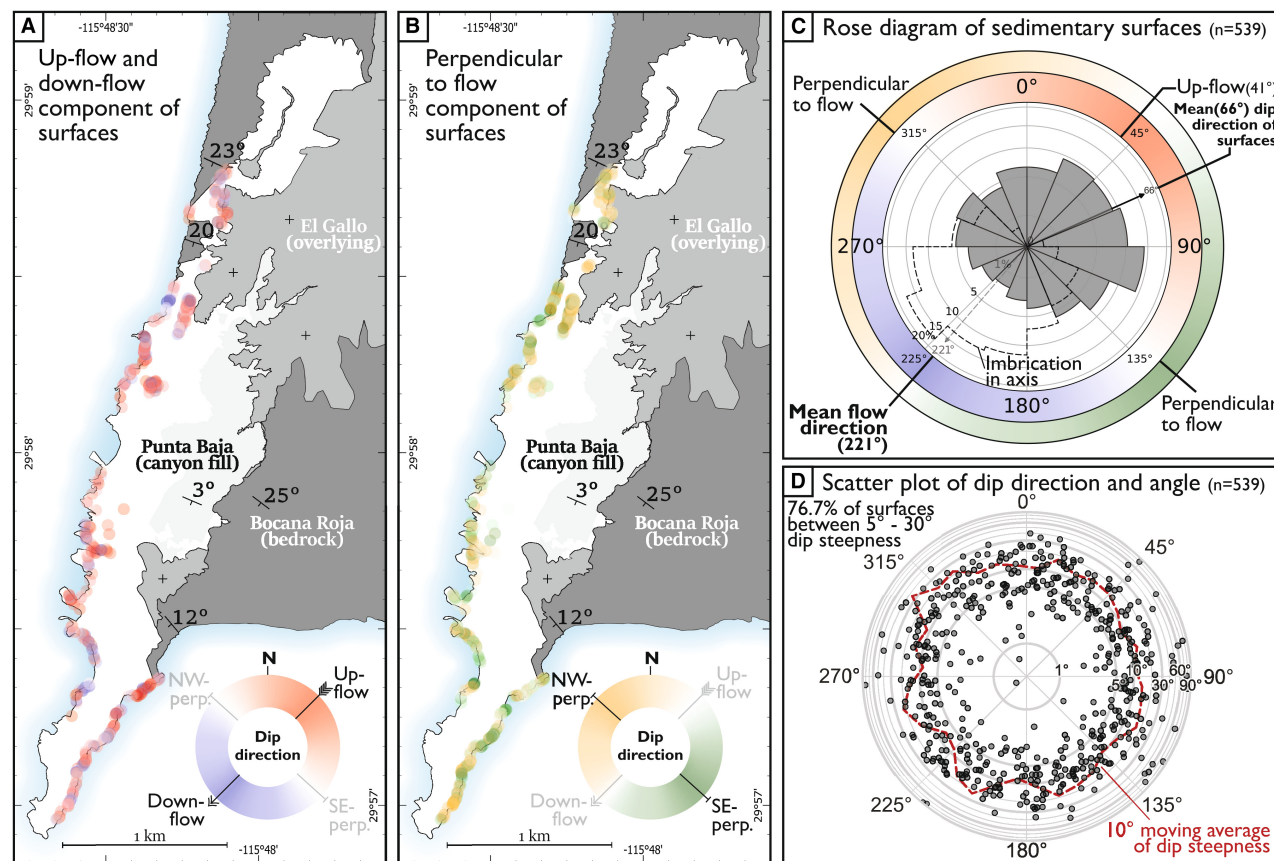
Fig. 15. Orientation and spatial distribution of 539 virtual three-dimensional outcrop model measured sedimentary surfaces in the Punta Baja conglomeratic canyon fill, compared with the mean sediment transport direction in axial conglomerate deposits. (A) Location of interpreted surfaces, coloured by dip direction relative to mean palaeoflow direction, focussing on up-stream and down-stream trends – see (C) for colour legend. Up-stream dipping surfaces dominate most locations, even with the canyon fill tectonic tilt dipping 3° downstream. (B) Location of the same interpreted surfaces, coloured by dip direction relative to mean palaeoflow direction, focussing on palaeoflow-perpendicular trends – see (C) for colour legend. Eastward and westward dipping surfaces occur evenly dispersed, suggesting no preferred orientation of flow-perpendicular surfaces. (C) Rose diagram comparing mean conglomerate imbrication transport direction (dashed, south-west 221° mean) to dip direction of sedimentary surfaces (grey, ENE 066° mean), showing a clear antithetic relation. The antithetic relation is supported by circular statistical analysis, where the surface orientations show a non-uniform (preferential) distribution with 99% confidence (Kuiper test at 99% confidence, Watson test at 95% confidence, Rayleigh test at 99% confidence; see Baas, 2000). (D) Scatter plot of dip direction and dip angle (note logarithmic radial axis) of sedimentary surfaces. More than 75% of sedimentary surfaces dip 5° to 30°, with no clear relation between dip direction and steepness, confirming that only the number of preserved surfaces dipping upstream is greater than downstream, and not the surface steepness.

et al., 2022). Where the surmounting sand-rich flows accelerated over the steep downstream part of the mass-transport complex, knickpoints or knickpoint zones could be initiated. Fining-up sandstone successions (<5 m thick) bounded by erosion surfaces atop mass-transport complexes (Fig. 14) could record deposition directly downstream of a migrating knickpoint. When these knickpoints, knickpoint zones or sand-rich channels were able to connect across the mass-transport deposit, a conduit was re-established

and gravel transport was resumed, evidenced by the return of conglomeratic axis deposits (Fig. 14).

The erosion by knickpoints and channels into the mud-rich mass-transport deposits would have resulted in increased mud content of flows, leading to mud-rich transitional flows downstream. The erosion rates due to knickpoint migration could also be instrumental in providing the near-bed sediment concentrations that are necessary for the development and migration
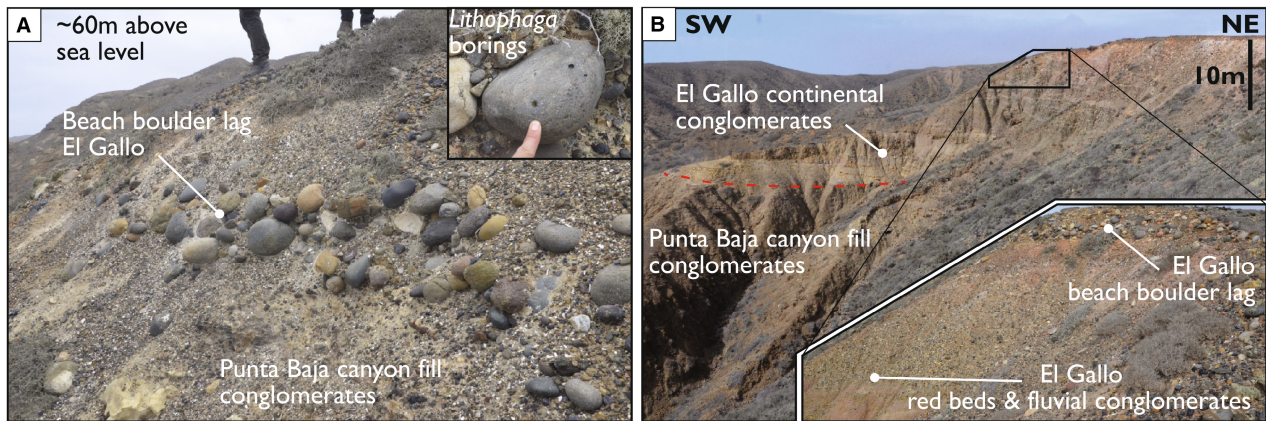
Fig. 16. Expression of the El Gallo unconformity. (A) A boulder bed directly overlying Punta Baja canyon-fill conglomerate deposits, containing bored clasts (inset). The clasts are very well-rounded. (B) A different expression of the unconformity where the boulder bed is preceded by red-weathering sandstones and conglomerates with angular clast of the El Gallo Formation.

of backsets (Englert *et al.*, 2023), which resulted in the upstream inclined surfaces (Fig. 15).

The dynamic erosional and depositional relief caused by mass-wasting events is thus a main factor in sediment capture and storage in submarine canyons, modifying downstream sediment delivery patterns and possibly overriding allogenic input signals.
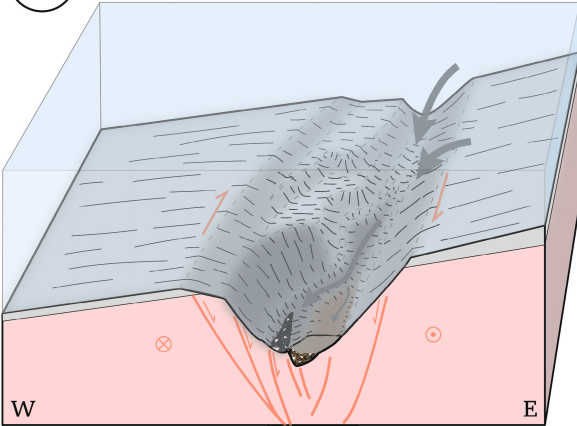
Proximality and flow filtering
The Punta Baja canyon fill stratigraphy has abundant large-scale erosion surfaces and thick, chaotic conglomerates (Fig. 6). This duality suggests an environment where large-scale catastrophic events eroded as well as deposited. Proximity to the canyon head could play an important role in the described stratigraphic expression of gravity flow activity and magnitude. The canyon head can act as a transient sediment storing site until catastrophic failure discharges large volumes of sediment down-canyon (Clare *et al.*, 2016; Bailey *et al.*, 2021; Talling *et al.*, 2023). The regions of sediment storage thus experience different patterns of erosion and deposition than their down-system reaches. The position and extent of the sediment storage site moves as the canyon evolves, shifting upstream in the case of a retrogressive canyon head. Other structures in canyons may have similar sediment storage and discharging effects, such as landslide dams (Pope *et al.*, 2022) or faults (Mountjoy *et al.*, 2009; Micallef *et al.*, 2014), which have a less predictable spatial and stratigraphic trajectory than canyon heads.
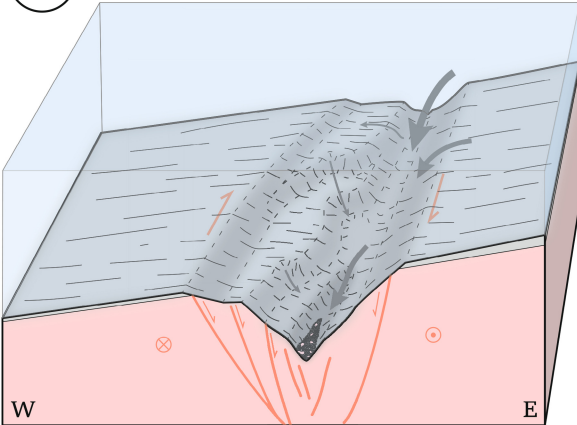
Stratigraphic evidence of this temporary sediment storage will be inherently difficult to identify, due to the catastrophic erosional nature of the remobilized sediment. The observed large-scale erosional surfaces and *en masse* deposited conglomerates may be interpreted as the record of large-magnitude canyon-flushing flows that likely originated by failure in the canyon head.

The confined overbank successions display a wide range of grain sizes and bed thicknesses, more varied in character compared to more distal and organized deep-water thin bed successions like external levées (Kane & Hodgson, 2011). Flows through canyons are rarely in equilibrium with the canyon gradient and intra-canyon confinement, and may either deposit updip of levéed channels, or are yet to bulk up and travel great distances (Heijnen *et al.*, 2022a) in contrast to lower slope and basin floor settings. Flow filtering may be enhanced downstream, as an initially wide range of starting flow magnitudes enter the overbank as a progressively narrow range due to updip overspill and intra-channel deposition (Prélat *et al.*, 2010), could mean that confined overbank deposits within submarine canyon fills provide a more complete stratigraphic record, this is unlikely given the degree of remobilization, erosion and reworking by bypassing flows. The limited role of flow filtering is illustrated in the present dataset by the characteristic wide range of grain sizes and bed thicknesses in canyon confined overbank deposits, which can support identification of these settings in subsurface datasets.
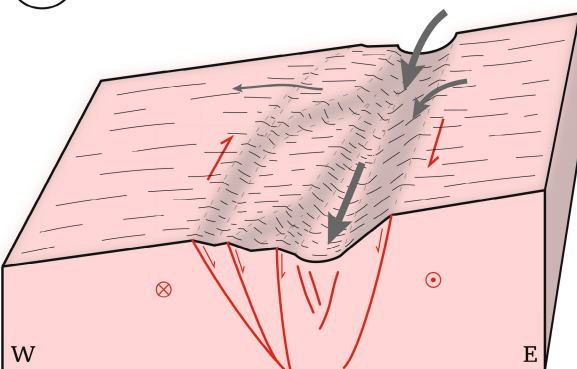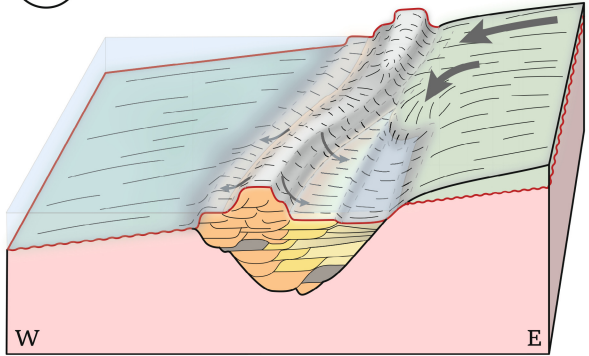
t6 **Exposure & ravinement**

t3 **Deepening & mass failure**

t5 **Widening & plugging**

t2 **Flooding & flow focussing**
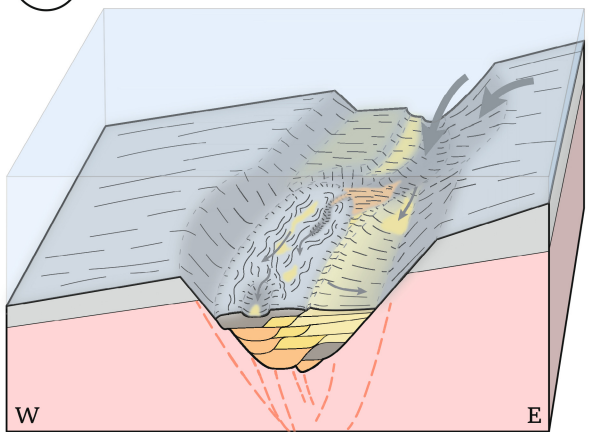
t4 **Widening & aggradation**

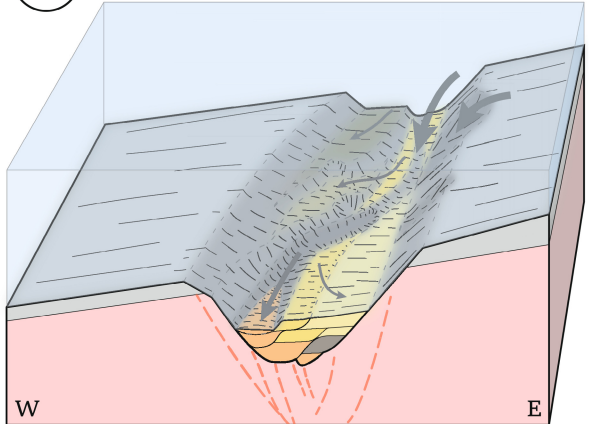**t1** **Tectonic fabric in fluvial bedrock**

Fig. 17. Evolutionary block diagrams of the Punta Baja canyon as a sediment conduit. (t1) – Bocana Roja Formation bedrock. Braided river and floodplain deposits from an eastward source. Releasing-bend tectonics create local depressions on the regional westward sloping basin margin. (t2) – Flooding of the basin margin. Submarine gravity flows are captured and focussed by the developing structural depression. Focussed, highly energetic flows erode and entrench the nascent canyon floor. (t3) – Erosional and tectonic deepening cause lateral and retrogressive canyon wall collapses. Most mass-wasting deposits are eroded in the high-gradient erosional canyon thalweg. Canyon widening allows flow expansion, flows become more depositional. Severe thalweg gradient changes caused by mass-wasting deposits induce knickpoint development. (t4) – Canyon widening and backstepping causes deposition and aggradation. Overbank developing in the form of canyon terraces. Thalweg migration through knickpoint migration leaves lateral step channel margin remnants. (t5) – Further canyon widening through flank collapse plugs thalweg, blocking and/or diverting flows. Canyon floor is wide enough for internal levée development. (t6) – Relative sea-level lowering, ravinement surface erodes an unknown thickness of canyon fill and bedrock. Differential weathering produces more erosion in overbank lithologies, where shallow marine and conglomeratic tallus sediments deposit.

CONCLUSIONS

In the area of Punta Baja, a bedrock-incised submarine canyon, with an asymmetrical coarse-grained axial fill and finer-grained canyon confined overbank deposits, is exposed. The structural and stratigraphic evolution of the Punta Baja submarine canyon is reconstructed from incision to fill:

- An inherited tectonic fabric influenced the location and orientation of canyon incision into fluvial bedrock.
- The depositional architecture of the north–south oriented erosionally confined canyon-fill is asymmetrical, with sub-vertically stacked channel-fills to the west, and an overbank confined by the canyon margin in the east.

Sedimentary process interactions led to depositional patterns that are considered characteristic of coarse-grained submarine canyon-fills:

- Evolving relief formed by mass-wasting processes captured sediment and may have driven knickpoint development, an autogenic mechanism that modifies sediment delivery to the ocean floor.
- This study interprets widespread upstream dipping surfaces in channel-fills as the stratigraphic expression of migrating supercritical-flow bedforms, such as cyclic steps (and possible sediment waves), which play an important role in sediment storage and transport in the canyon.
- The proximal location of submarine canyons limits the filtering of the initial wide range of gravity flow types, creating poorly-organised depositional patterns, including scours and bypass lags, in the intra-canyon overbank areas.

- The canyon remained an active coarse-grained sediment conduit throughout the time represented by the preserved fill.

This study provides insights into how processes that are observed in modern canyons are selectively preserved through the lifetime of the canyon and construct or destroy stratigraphy on geological timescales.

ACKNOWLEDGEMENTS

DATA AVAILABILITY STATEMENT

The data that supports the findings of this study are available in the Supporting Information of this article.

REFERENCES

Abreu, V., **Sullivan, M.**, **Pirmez, C.** and **Mohrig, D.** (2003) Lateral accretion packages (LAPs): an important reservoir element in deep water sinuous channels. *Mar. Pet. Geol.*, **20**, 631–648.

Advocate, D.M., **Link, M.H.** and **Squires, R.L.** (1988) Anatomy and history of an Eocene Submarine Canyon: the Maniobra Formation, Southern California. In: *Paleogene Stratigraphy, West Coast of North America* (Eds Filewicz, M.V. and Squires, R.L.). 45–58. Pacific Section, SEPM, Los Angeles.

Allen, S.E. and **Durrieu De Madron, X.** (2009) A review of the role of submarine canyons in deep-ocean exchange with the shelf. *Ocean Sci.*, **5**, 607–620.

Allen, C., **Gomis-Cartesio, L.E.**, **Hodgson, D.M.**, **Peakall, J.** and **Milana, J.** (2022) Channel incision into a submarine landslide on a Carboniferous basin margin, San Juan, Argentina: evidence for the role of knickpoints. *Depositional Rec.*, **8**, 628–655.

Allmendinger, R.W., **Cardozo, N.** and **Fischer, D.M.** (2013) *Structural Geology Algorithms: Vectors and Tensors.* Cambridge University Press, Cambridge.

Almgren, A.A. and **Hacker, P.D.** (1984) *Paleogene Submarine Canyons of the Sacramento Valley, California.* Pacific Section American Association of Petroleum Geologists, Los Angeles.

Alsleben, H., **Wetmore, P.H.**, **Gehrels, G.E.** and **Paterson, S.R.** (2012) Detrital zircon ages in Palaeozoic and Mesozoic basement assemblages of the Peninsular Ranges batholith, Baja California, Mexico: constraints for depositional ages and provenance. *Int. Geol. Rev.*, **54**, 93–110.

Aslam, T., **Hall, R.A.** and **Dye, S.R.** (2018) Internal tides in a dendritic submarine canyon. *Prog. Oceanogr.*, **169**, 20–32.

Azpiroz-Zabala, M., **Cartigny, M.J.B.**, **Talling, P.J.**, **Parsons, D.R.**, **Sumner, E.J.**, **Clare, M.A.**, **Simmons, S.M.**, **Cooper, C.** and **Pope, E.L.** (2017) Newly recognized turbidity current structure can explain prolonged flushing of submarine canyons. *Sci. Adv.*, **3**, 1–12.

Baas, J.H. (2000) EZ-ROSE: a computer program for equal-area circular histograms and statistical analysis of two-dimensional vectorial data. *Comput. Geosci.*, **26**, 153–166.

Baas, J.H., **Best, J.L.** and **Peakall, J.** (2011) Depositional processes, bedform development and hybrid bed formation in rapidly decelerated cohesive (mud–sand) sediment flows. *Sedimentology*, **58**, 1953–1987.

Bailey, L.P., **Clare, M.A.**, **Rosenberger, K.J.**, **Cartigny, M.J.B.**, **Talling, P.J.**, **Paull, C.K.**, **Gwiazda, R.**, **Parsons, D.R.**, **Simmons, S.M.**, **Xu, J.**, **Haigh, I.D.**, **Maier, K.L.**, **Mcgann, M.**, **Lundsten, E.** and **Team, M.C.** (2021) Preconditioning by sediment accumulation can produce powerful turbidity currents without major external triggers. *Earth Planet. Sci. Lett.*, **562**, 116845.

Beal, C.H. (1948) Geology and Oil Possibilities of Baja California, Mexico. *Geol. Soc. Am.*, **31**, 1–138.

Bianchelli, S., **Gambi, C.**, **Zeppilli, D.** and **Danovaro, R.** (2010) Metazoan meiofauna in deep-sea canyons and adjacent open slopes: a large-scale comparison with focus on the rare taxa. *Deep Sea Res. Part I Oceanogr. Res. Pap.*, **57**, 420–433.

Boehlke, J.E. and **Abbott, P.L.** (1986) Punta Baja Formation, A Campanian Submarine Canyon Fill, Baja California, Mexico. In: *Cretaceous Stratigraphy Western North America: Los Angeles, Pacific Section* (Ed Abott, P.L.), *Society for Economic Paleontologists and Mineralogists*, Book **46**, 91–101. SEPM Society for Sedimentary Geology, Los Angeles.

Boulesteix, K., **Poyatos-Moré, M.**, **Flint, S.S.**, **Taylor, K.G.**, **Hodgson, D.M.** and **Hasiotis, S.T.** (2019) Transport and deposition of mud in deep-water environments: processes and stratigraphic implications. *Sedimentology*, **66**, 2894–2925.

Bouma, A.H. (1962) *Sedimentology of Some Flysch Deposits.* Elsevier Scientific Publishing Company, Amsterdam.

Brunt, R.L., **Hodgson, D.M.**, **Flint, S.S.**, **Pringle, J.K.**, **Di Celma, C.**, **Prélat, A.** and **Grecula, M.** (2013) Confined to unconfined: anatomy of a base of slope succession, Karoo Basin, South Africa. *Mar. Pet. Geol.*, **41**, 206–221.

Buckley, S.J., **Ringdal, K.**, **Naumann, N.**, **Dolva, B.**, **Kurz, T.H.**, **Howell, J.A.** and **Dewez, T.J.B.** (2019) LIME: software for 3-D visualization, interpretation, and communication of virtual geoscience models. *Geosphere*, **15**, 222–235.

Busby, C.J., **Smith, D.**, **Morris, W.** and **Fackler-Adams, B.** (1998) Evolutionary model for convergent margins facing large ocean basins: Mesozoic Baja California, Mexico. *Geology*, **26**, 227–230.

Busby, C.J., **Fackler Adams, B.**, **Mattinson, J.** and **Deoreo, S.** (2006) View of an intact oceanic arc, from surficial to mesozonal levels: cretaceous Alisitos arc, Baja California. *J. Volcanol. Geotherm. Res.*, **149**, 1–46.

Campbell, C.V. (1967) Lamina, laminaset, bed and bedset. *Sedimentology*, **8**, 7–26.

Cardozo, N. and **Allmendinger, R.W.** (2013) Spherical projections with OSXStereonet. *Comput. Geosci.*, **51**, 193–205.

Cartigny, M.J., **Postma, G.**, **van den Berg, J.H.** and **Mastbergen, D.R.** (2011) A comparative study of sediment waves and cyclic steps based on geometries, internal structures and numerical modeling. *Mar. Geol.*, **28**, 40–56.

Christie-Blick, N. and **Biddle, K.T.** (1985) Deformation and basin formation along strike-slip faults. In: *Strike-Slip Deformation, Basin Formation, and Sedimentation* (Eds Biddle, K.T. and Christie-Blick, N.), SEPM Special Publications no. 37, 1–34. SEPM, Tulsa.

Clare, M.A., **Hughes Clarke, J.E.**, **Talling, P.J.**, **Cartigny, M.J.B.** and **Pratomo, D.G.** (2016) Preconditioning and triggering of offshore slope failures and turbidity currents revealed by most detailed monitoring yet at a fjord-head delta. *Earth Planet. Sci. Lett.*, **450**, 208–220.

Clare, M., **Hunt, J.**, **Kane, I.**, **Fonnesu, M.**, **Malgesini, G.** and **Bailey, L.** (2023) Instability of Deep-Sea Currents over Tidal and Seasonal Timescales. pp. 1–19.

Clifton, H.E. (1984) Sedimentation units in stratified resedimented conglomerate, Paleocene submarine canyon fill, Point Lobos, California. In: *Sedimentology of Gravels and Conglomerates* (Eds Koster, E.H. and Steel, R.J.), **10**, 429–441. Canadian Society of Petroleum Geologists, Memoir, Calgary.

Clifton, H.E. and **Hill, G.W.** (1987) Paleocene submarine-canyon fill, Point Lobos, California. *Cordilleran Section: Geological Society of America Centennial Field Guide*, **1**, 239–244.

Cronin, B.T. (2018) Lithofabric classification and distribution of coarse-grained deep-water clastic depositional systems. In: *Rift-Related Coarse-Grained Submarine Fan Reservoirs; the Brae Play, South Viking Graben, North Sea: AAPG Memoir 115* (Eds Turner, C.C. and Cronin, B.T.), pp. 39–96. American Association of Petroleum Geologists, Tulsa.

Cronin, B.T. and **Kidd, R.B.** (1998) Heterogeneity and lithotype distribution in ancient deep-sea canyons: point Lobos deep-sea canyon as a reservoir analogue. *Sed. Geol.*, **115**, 315–349.

Dailly, G.C. (1982) Slope readjustment during sedimentation on continental margins. In: *Studies in Continental Margin Geology* (Eds Watkins, J.S. and Drake, C.L.). American Association of Petroleum Geologists, Tulsa.

Dakin, N., Pickering, K.T., Mohrig, D. and Bayliss, N.J. (2013) Channel-like features created by erosive submarine debris flows: field evidence from the Middle Eocene Ainsa Basin, Spanish Pyrenees. *Mar. Pet. Geol.*, 41, 62–71.

Daly, R.A. (1936) Origin of submarine canyons. *Am. J. Sci.*, 31, 401–420.

Dasgupta, S. and Buatois, L.A. (2015) High-frequency stacking pattern and stages of canyon/gully evolution across a forced regressive shelf-edge delta-front. *Mar. Pet. Geol.*, 68, 40–53.

Di Celma, C. and Cantalamessa, G. (2012) Off-shelf sedimentary record of recurring global sea-level changes during the Plio-Pleistocene: evidence from the cyclic fills of exhumed slope systems in central Italy. *J. Geol. Soc. Lond.*, 169, 643–646.

Dickinson, W.R. and Gehrels, G.E. (2009) U-Pb ages of detrital zircons in Jurassic eolian and associated sandstones of the Colorado Plateau: evidence for transcontinental dispersal and intraregional recycling of sediment. *Geol. Soc. Am. Bull.*, 121, 408–433.

Dresen, G. (1991) Stress distribution and the orientation of Riedel shears. *Tectonophysics*, 188, 239–247.

Edwards, D.A., Leeder, M.R., Best, J.L. and Pantin, H.M. (1994) On experimental reflected density currents and the interpretation of certain turbidites. *Sedimentology*, 41, 437–461.

Englert, R.G., Vellinga, A.J., Cartigny, M.J.B., Clare, M.A. and Eggenhuisen, J.T. (2023) Controls on upstream-migrating bed forms in sandy submarine channels. *Geology*, 51, 1137–1142.

Fastovsky, D.E., Montellano-ballesteros, M., Fricke, H.C., Ramezani, J., Tsukui, K., Wilson, G.P., Hall, P., Hernandez-Rivera, R. and Alvarez, G. (2020) Paleoenvironments, taphonomy, and stable isotopic content of the terrestrial, fossil-vertebrate–bearing sequence of the El Disecado Member, El Gallo Formation, Upper Cretaceous, Baja California, México. *Geosphere*, 16, 1–21.

Fernandez-Arcaya, U., Ramirez-Llodra, E., Aguzzi, J., Allcock, A.L., Davies, J.S., Dissanayake, A., Harris, P., Howell, K., Huvenne, V.A.I., Macmillan-Lawler, M., Martín, J., Menot, L., Nizinski, M., Puig, P., Rowden, A.A., Sanchez, F. and van den Beld, I.M.J. (2017) Ecological role of submarine canyonsand need for canyon conservation: a review. *Front. Mar. Sci.*, 4, 1–26.

Fildani, A. (2017) Submarine canyons: a brief review looking forward. *Geology*, 45, 383–384.

Fisher, W.L., Galloway, W.E., Steel, R.J., Olariu, C., Kerans, C. and Mohrig, D. (2021) Deep-water depositional systems supplied by shelf-incising submarine canyons: recognition and significance in the geologic record. *Earth Sci. Rev.*, 214, 103531.

FitzGerald, M.S. and Gorsline, D.S. (1989) Clast-contact conglomerates in submarine canyon fill: possible subaqueous sieve deposits, Carmelo Formation (Paleocene), Point Lobos, California. Conglomerates in Basin Analysis, A symposium dedicated to A. O. Woodford. Pacific Section SEPM, 62, pp. 99-111. *Planet. Sci. Lett.*, 450, 208–220.

Galloway, W.E., Dingus, W.F. and Paige, R.E. (1991) Seismic and depositional facies of paleocene-eocene wilcox group submarine canyon fills, Northwest Gulf Coast, U.S.A. In: *Seismic Facies and Sedimentary Processes of Submarine Fans and Turbidite Systems* (Eds Weimer, P. and Link, M.H.), Frontiers in Sed. Geol., 247–271. Springer Science+Business Media, New York.

Gastil, R.G., Phillips, R.P. and Allison, E.C. (1971) Reconnaissance geologicmap of the State of Baja California, scale 1:250 000. *Mem. Geol. Soc. Am.*, 140, 179.

Gastil, R.G., Phillips, R.P. and Allison, E.C. (1975) Reconnaissance geology of the State of Baja California. *Geol. Soc. Am. Mem.*, 140, 1–201.

Gong, C., Wang, Y., Zhu, W., Li, W., Xu, Q. and Zhang, J. (2011) The central submarine canyon in the qiongdongnan basin, northwestern south China sea: architecture, sequence stratigraphy, and depositional processes. *Mar. Pet. Geol.*, 28, 1690–1702.

Guiastrennec-Faugas, L., Gillet, H., Jacinto, R.S., Dennielou, B., Hanquiez, V., Schmidt, S., Simplet, L. and Rousset, A. (2020) Upstream migrating knickpoints and related sedimentary processes in a submarine canyon from a rare 20-year morphobathymetric time-lapse (Capbreton submarine canyon, Bay of Biscay, France). *Mar. Geol.*, 423, 106–143.

Hage, S., Cartigny, M.J., Clare, M.A., Sumner, E.J., Vendettuoli, D., Clarke, J.E.H., Hubbard, S.M., Talling, P.J., Lintern, D.G., Stacey, C.D. and Englert, R.G. (2018) How to recognize crescentic bedforms formed by supercritical turbidity currents in the geologic record: insights from active submarine channels. *Geology*, 46, 563–566.

Hage, S., Galy, V.V., Cartigny, M.J.B., Acikalin, S., Clare, M.A., Gröcke, D.R., Hilton, R.G., Hunt, J.E., Lintern, D.G., McGhee, C.A., Parsons, D.R., Stacey, C.D., Sumner, E.J. and Talling, P.J. (2020) Efficient preservation of young terrestrial organic carbon in sandy turbidity-current deposits. *Geology*, 48, 882–887.

Hagstrum, J.T., McWilliams, M., Howell, D.G. and Gromme, S. (1985) Mesozoic paleomagnetism and northward translation of the Baja California Peninsula. *Geol. Soc. Am. Bull.*, 96, 1077–1090.

Hand, B.M. (1974) Supercritical flow in density currents. SEPM J. Sediment. Res., 44, 637–648.

Harms, J.C. (1969) Hydraulic significance of some sand ripples. *GSA Bull.*, 80, 363–396.

Harris, P.T., Macmillan-Lawler, M., Rupp, J. and Baker, E.K. (2014) Geomorphology of the oceans. *Mar. Geol.*, 352, 4–24.

Heijnen, M.S., Clare, M.A., Cartigny, M.J.B., Talling, P.J., Hage, S., Pope, E.L., Bailey, L., Sumner, E., Gwyn Lintern, D., Stacey, C., Parsons, D.R., Simmons, S.M., Chen, Y., Hubbard, S.M., Eggenhuisen, J.T., Kane, I. and Hughes Clarke, J.E. (2022a) Fill, flush or shuffle: how is sediment carried through submarine channels to build lobes? *Earth Planet. Sci. Lett.*, 584, 1–14.

Heijnen, M.S., Mienis, F., Gates, A.R., Bett, B.J., Hall, R.A., Hunt, J., Kane, I.A., Pebody, C., Huvenne, V.A.I., Soutter, E.L. and Clare, M.A. (2022b) Challenging the highstand-dormant paradigm for land-detached submarine canyons. *Nat. Commun.*, 13, 3448.

Hein, F.J. (1984) Deep-sea and fluvial braided channel conglomerates: a comparison of two case studies. In: *Sedimentology of Gravels and Conglomerates* (Eds Koster, E.H. and Steel, R.J.), 10, 33–49. Canadian Society of Petroleum Geologists, Memoir, Calgary.

Hein, F.J. and Walker, R.G. (1991) The Cambro-Ordovician cap enragé formation, Québec, Canada: conglomeratic deposits of a braided submarine channel with terraces. In: *Deep-Water Turbidite Systems*, pp. 231–251. Wiley, Oxford, UK.

Hesse, R., Klaucke, I., Khodabakhsh, S., Piper, D.J.W. and Ryan, W.B.F. (2001) Sandy submarine braid plains: potential deep-water reservoirs. *Am. Assoc. Pet. Geol. Bull.*, **85**, 1499–1521.

Hiscott, R.N. and Pickering, K.T. (1984) Reflected turbidity currents on an Ordovician basin floor, Canadian Appalachians. *Nature*, **311**, 143–145.

Hsieh, Y., Liu, C., Suppe, J., Byrne, T.B. and Lallemand, S. (2020) The Chimei Submarine Canyon and Fan: a record of Taiwan arc-continent collision on the rapidly deforming overriding plate. *Tectonics*, **39**, 1–36.

Huang, L. and Liu, C.Y. (2017) Three types of flower structures in a divergent-wrench fault zone. *J. Geophys. Res. Solid Earth*, **122**, 10478–10497.

Ito, M. and Saito, T. (2006) Gravel waves in an Ancient Canyon: analogous features and formative processes of coarse-grained bedforms in a submarine-fan system, the lower pleistocene of the Boso Peninsula, Japan. *J. Sediment. Res.*, **76**, 1274–1283.

Ito, M., Ishikawa, K. and Nishida, N. (2014) Distinctive erosional and depositional structures formed at a canyon mouth: a lower Pleistocene deep-water succession in the Kazusa forearc basin on the Boso Peninsula, Japan. *Sedimentology*, **61**, 2042–2062.

Janocko, J. and Basilici, G. (2021) Architecture of coarse-grained gravity flow deposits in a structurally confined submarine canyon (late Eocene Tokaren Conglomerate, Slovakia). *Sediment. Geol.*, **417**, 105880.

Kamb, W.B. (1959) Ice petrofabric observations from Blue Glacier, Washington, in relation to theory and experiment. *J. Geophys. Res.*, **64**, 1891–1909.

Kane, I.A. and Hodgson, D.M. (2011) Sedimentological criteria to differentiate submarine channel levee subenvironments: exhumed examples from the Rosario Fm. (Upper Cretaceous) of Baja California, Mexico, and the Fort Brown Fm. (Permian), Karoo Basin, S. Africa. *Mar. Pet. Geol.*, **28**, 807–823.

Kane, I.A., McCaffrey, W.D. and Peakall, J. (2010) On the origin of paleocurrent complexity within deep marine channel levees. *J. Sediment. Res.*, **80**, 54–66.

Kane, I.A., Hodgson, D.M., Hubbard, S.M., McArthur, A.D., Poyatos-Moré, M., Soutter, E.L., Flint, S.S. and Matthews, W. (2022) Deep-water Tectono-Stratigraphy at a plate boundary constrained by large N-Detrital Zircon and micropaleontological approaches: Peninsular Ranges Forearc, Baja California, Mexico. *Sediment. Rec.*, **20**, 37652.

Katz, Y., Weinberger, R. and Aydin, A. (2004) Geometry and kinematic evolution of Riedel shear structures, Capitol Reef National Park, Utah. *J. Struct. Geol.*, **26**, 491–501.

Kilmer, F.H. (1963) *Cretaceous and cenozoic stratigraphy and paleontology, El Rosario Area, Baja California, Mexico*. University of California, Berkeley.

Klaucke, I. and Hesse, R. (1996) Fluvial features in the deep-sea: new insights from the glacigenic submarine drainage system of the Northwest Atlantic Mid-Ocean Channel in the Labrador Sea. *Sediment. Geol.*, **106**, 223–234.

Knaust, D. (2019) The enigmatic trace fossil Tisoa Serres, 1840. *Earth-Sci. Rev.*, **188**, 123–147.

Kneller, B., Edwards, D., McCaffrey, W. and Moore, R. (1991) Oblique reflection of turbidity currents. *Geology*, **19**, 250–252.

Komar, P.D. (1971) Hydraulic jumps in turbidity currents. *Bull. Geol. Soc. Am.*, **82**, 1477–1488.

Kuenen, P.H. (1938) Density currents in connection with the problem of Submarine Canyons. *Geol. Mag.*, **75**, 241–249.

Lastras, G., Canals, M., Urgeles, R., Amblas, D., Ivanov, M., Droz, L., Dennielou, B., Fabrés, J., Schoolmeester, T., Akhmetzhanov, A. and Orange, D. (2007) A walk down the Cap de Creus canyon, Northwestern Mediterranean Sea: recent processes inferred from morphology and sediment bedforms. *Mar. Geol.*, **246**, 176–192.

Lastras, G., Arzola, R.G., Masson, D.G., Wynn, R.B., Huvenne, V.A.I., Hühnerbach, V. and Canals, M. (2009) Geomorphology and sedimentary features in the Central Portuguese submarine canyons, Western Iberian margin. *Geomorphology*, **103**, 310–329.

Li, M.Z., Prescott, R.H. and Robertson, A.G. (2019) Observation of internal tides and sediment transport processes at the head of Logan Canyon on central Scotian Slope, eastern Canada. *J. Mar. Syst.*, **193**, 103–125.

Li, Y., Pu, R., Zhang, G., Zhao, X. and Li, Y. (2022) Architecture, controlling factors and evolution history of unidirectionally upstream-migrating turbidite channels: a case study from southern Qiongdongnan Basin, northern South China Sea. *Mar. Pet. Geol.*, **141**, 105706.

Liang, C., Liu, C., Xie, X., Yu, X., He, Y., Chen, H., Zhou, Z., Tian, D., Lu, B., Mi, H., Li, M., Zhang, H. and Yang, Y. (2020) The role of large-scale mass wasting processes in changing the sediment dispersal pattern in the deep-water Central Canyon of the northwestern South China Sea. *Mar. Pet. Geol.*, **122**, 104693.

Lo Iacono, C., Guillén, J., Guerrero, Q., Durán, R., Wardell, C., Hall, R.A., Aslam, T., Carter, G.D.O., Gales, J.A. and Huvenne, V.A.I. (2020) Bidirectional bedform fields at the head of a submarine canyon (NE Atlantic). *Earth Planet. Sci. Lett.*, **542**, 116321.

Lowe, D.R. (1982) Sediment gravity flows: II depositional models with special reference to the deposits of high-density turbidity currents. *J. Sed. Petrol.*, **52**, 279–297.

Martínez-Doñate, A., Privat, A.M.-L.J., Hodgson, D.M., Jackson, C.A.L., Kane, I.A., Spychala, Y.T., Duller, R.A., Stevenson, C., Keavney, E., Schwarz, E. and Flint, S.S. (2021) Substrate entrainment, depositional relief, and sediment capture: impact of a submarine landslide on flow process and sediment supply. *Front. Earth Sci.*, **9**, 1–23.

Matthews, W.A. and Guest, B. (2016) A practical approach for collecting large- n detrital zircon U-Pb data sets by quadrupole LA - ICP - MS. *Geostand. Geoanal. Res.*, **41**, 161–180.

May, J.A. and Warme, J.A. (2007) An ancient submarine Canyon, Black's Beach, La Jolla, California, USA. In: *Atlas of Deep-Water Outcrops: AAPG Studies in Geology 56* (Eds Nilsen, T.H., Shew, R.D., Steffens, G.S. and Studlick, J.R.J.). The American Association of Petroleum Geologists, Tulsa.

McArthur, A.D. and McCaffrey, W.D. (2019) Sedimentary architecture of detached deep-marine canyons: examples from the East Coast Basin of New Zealand. *Sedimentology*, **66**, 1067–1101.

McArthur, A., Kane, I., Bozetti, G., Hansen, L. and Kneller, B.C. (2020) Supercritical flows overspilling from bypass-dominated submarine channels and the development of overbank bedforms. *Depositional Rec.*, **6**, 21–40.

Micallef, A., Mountjoy, J.J., Barnes, P.M., Canals, M. and Lastras, G. (2014) Geomorphic response of submarine canyons to tectonic activity: insights from the Cook Strait canyon system, New Zealand. *Geosphere*, **10**, 905–929.

Millington, J.J. and **Clark, J.D.** (1995) The charo/arro canyon-mouth sheet system, South-Central Pyrenees, Spain: a structurally influenced zone of sediment dispersal. *J. Sed. Res.*, **65**, 443–454.

Misra, S., **Mandal, N.** and **Chakraborty, C.** (2009) Formation of Riedel shear fractures in granular materials: findings from analogue shear experiments and theoretical analyses. *Tectonophysics*, **471**, 253–259.

Morris, W.R. and **Busby, C.J.** (1996) The effects of tectonism on the high resolution sequence stratigraphic framework of non-marine to deep-marine deposits in the Peninsular Ranges forearc basin complex. In: *Field Conference Guide 1996. Pacific Section A.A.P.G* (Eds Abott, P.L. and Cooper, J.D.), *Pacific Section S.E.P.M.*, 381–408. SEPM Society for Sedimentary Geology, Los Angeles.

Morris, W.R. and **Busby-Spera, C.J.** (1988) Sedimentologic evolution of a submarine canyon in a forearc basin, Upper Cretaceous Rosario Formation, San Carlos, Mexico. *Am. Assoc. Pet. Geol. Bull.*, **72**, 717–737.

Mountjoy, J.J., **Barnes, P.M.** and **Pettinga, J.R.** (2009) Morphostructure and evolution of submarine canyons across an active margin: cook strait sector of the Hikurangi Margin, New Zealand. *Mar. Geol.*, **260**, 45–68.

Mutti, E. (1992) Turbidite sandstones. *Agip S.p.A.*, S. Donato Milanese.

Nazarian, R.H., **Burns, C.M.**, **Legg, S.**, **Buijsman, M.C.**, **Kaur, H.** and **Arbic, B.K.** (2021) On the magnitude of canyon-induced mixing. *J. Geophys. Res. Ocean.*, **126**, 1–16.

Nemec, W. (1988) The shape of the rose. *Sediment. Geol.*, **59**, 149–152.

Nemec, W. (1990) Aspects of sediment movement on steep delta slopes. In: *Coarse-Grained Deltas*, pp. 29–73. Blackwell Publishing Ltd., Oxford, UK.

Normandeau, A., **Dafoe, L.T.**, **Li, M.Z.**, **Campbell, D.C.** and **Jenner, K.A.** (2024) Sedimentary record of bottom currents and internal tides in a modern highstand submarine canyon head. *Sedimentology*, **71**, 1061–1083.

Normark, W.R. and **Piper, D.J.W.** (1991) Initiation processes and flow evolution of turbidity currents: implications for the depositional record. In: *From Shoreline to Abyss: Contributions in Marine Geology in Honor of Francis Parker Shepard* (Ed Osborne, R.H.), **46**, 207–230. SEPM Society for Sedimentary Geology, Tulsa.

Normark, W.R., **Posamentier, H.** and **Mutti, E.** (1993) Turbidite systems: state of the art and future directions. *Rev. Geophys.*, **31**, 91–116.

Palanques, A., **Masqué, P.**, **Puig, P.**, **Sanchez-Cabeza, J.A.**, **Frignani, M.** and **Alvisi, F.** (2008) Anthropogenic trace metals in the sedimentary record of the Llobregat continental shelf and adjacent Foix Submarine Canyon (northwestern Mediterranean). *Mar. Geol.*, **248**, 213–227.

Paull, C.K., **Talling, P.J.**, **Maier, K.L.**, **Parsons, D.**, **Xu, J.**, **Caress, D.W.**, **Gwiazda, R.**, **Lundsten, E.M.**, **Anderson, K.**, **Barry, J.P.**, **Chaffey, M.**, **O'Reilly, T.**, **Rosenberger, K.J.**, **Gales, J.A.**, **Kieft, B.**, **McGann, M.**, **Simmons, S.M.**, **McCann, M.**, **Sumner, E.J.**, **Clare, M.A.** and **Cartigny, M.J.** (2018) Powerful turbidity currents driven by dense basal layers. *Nat. Commun.*, **9**, 4114.

Pham, C.K., **Ramirez-Llodra, E.**, **Alt, C.H.S.**, **Amaro, T.**, **Bergmann, M.**, **Canals, M.**, **Company, J.B.**, **Davies, J.**, **Duineveld, G.**, **Galgani, F.**, **Howell, K.L.**, **Huvenne, V.A.I.**, **Isidro, E.**, **Jones, D.O.B.**, **Lastras, G.**, **Morato, T.**, **Gomes-Pereira, J.N.**, **Purser, A.**, **Stewart, H.**, **Tojeira, I.**, **Tubau, X.**, **Van Rooij, D.** and **Tyler, P.A.** (2014) Marine litter distribution and density in European seas, from the shelves to deep basins. *PLoS One*, **9**, e95839.

Piper, D.J.W. and **Kontopoulos, N.** (1994) Bed forms in submarine channels: comparison of ancient examples from greece with studies of recent turbidite systems. *SEPM J. Sed. Res.*, **64**, 247–252.

Pope, E.L., **Heijnen, M.S.**, **Talling, P.J.**, **Jacinto, R.S.**, **Gaillot, A.**, **Baker, M.L.**, **Hage, S.**, **Hasenhündl, M.**, **Heerema, C.J.**, **McGhee, C.**, **Ruffell, S.C.**, **Simmons, S.M.**, **Cartigny, M.J.B.**, **Clare, M.A.**, **Dennielou, B.**, **Parsons, D.R.**, **Peirce, C.** and **Urlaub, M.** (2022) Carbon and sediment fluxes inhibited in the submarine Congo Canyon by landslide-damming. *Nat. Geosci.*, **15**, 845–853.

Postma, G. and **Cartigny, M.J.B.** (2014) Supercritical and subcritical turbidity currents and their deposits—a synthesis. *Geology*, **42**, 987–990.

Postma, G., **Nemec, W.** and **Kleinspehn, K.L.** (1988) Large floating clasts in turbidites: a mechanism for their emplacement. *Sed. Geol.*, **58**, 47–61.

Prélat, A., **Covault, J.A.**, **Hodgson, D.M.**, **Fildani, A.** and **Flint, S.S.** (2010) Intrinsic controls on the range of volumes, morphologies, and dimensions of submarine lobes. *Sed. Geol.*, **232**, 66–76.

Puig, P., **Palanques, A.**, **Guillén, J.** and **El Khatab, M.** (2004) Role of internal waves in the generation of nepheloid layers on the northwestern Alboran slope: implications for continental margin shaping. *J. Geophys. Res. Ocean.*, **109**, 1–11.

Puig, P., **Palanques, A.** and **Martín, J.** (2014) Contemporary SEDIMENT-TRANSPORT PROCESSES in Submarine Canyons. *Annu. Rev. Mar. Sci.*, **6**, 53–77.

Rasmussen, E.S. (1994) The relationship between submarine canyon fill and sea-level change: an example from Middle Miocene offshore Gabon, West Africa. *Sed. Geol.*, **90**, 61–75.

Reading, H.G. (1980) Characteristics and recognition of strike-slip fault systems. In: *Sedimentation in Oblique-Slip Mobile Zones* (Eds Ballance, P.F. and Reading, H.G.), The International Association of Sedimentologists, 7–26. Blackwell Scientific Publications, Oxford.

Reading, H.G. (Ed) (1996) *Sedimentary Environments: Processes, Facies, and Stratigraphy*, 3rd edn. Blackwell Publishing, Oxford.

Rodgers, D.A. (1980) Analysis of pull-apart basin development produced by en echelon strike-slip faults. In: *Sedimentation in Oblique-Slip Mobile Zones* (Eds Ballance, P.F. and Reading, H.G.), The International Association of Sedimentologists, 27–41. Blackwell Scientific Publications, Oxford.

Rutter, E.H., **Maddock, R.H.**, **Hall, S.H.** and **White, S.H.** (1986) Comparative microstructures of natural and experimentally produced clay-bearing fault gouges. *Pure Appl. Geophys. PAGEOPH*, **124**, 3–30.

Schile, C.A. (1974) *Sedimentology of the "El Gallo Formation" (Upper Cretaceous), El Rosario, Baja California, Mexico*. San Diego State University, San Diego.

Schlacher, T., **Schlacher-Hoenlinger, M.**, **Williams, A.**, **Althaus, F.**, **Hooper, J.** and **Kloser, R.** (2007) Richness and distribution of sponge megabenthos in continental margin canyons off southeastern Australia. *Mar. Ecol. Prog. Ser.*, **340**, 73–88.

Seidler, L. (2000) Incised submarine canyons governing new evidence of Early Triassic rifting in East Greenland. *Palaeogeogr. Palaeoclimatol. Palaeoecol.*, **161**, 267–293.

Sharman, G.R., **Sharman, J.P.** and **Sylvester, Z.** (2018) detritalPy: a Python-based toolset for visualizing and

analysing detrital geo-thermochronologic data. *Depositional Rec.*, **4**, 202–215.

Shepard, F.P. (1972) Submarine canyons. *Earth-Sci. Rev.*, **8**, 1–12.

Spencer, C.J., **Kirkland, C.L.** and **Taylor, R.J.M.** (2016) Strategies towards statistically robust interpretations of in situ U–Pb zircon geochronology. *Geosci. Front.*, **7**, 581–589.

Stevenson, C.J., **Jackson, C.A.-L.**, **Hodgson, D.M.**, **Hubbard, S.M.** and **Eggenhuisen, J.T.** (2015) Deep-water sediment bypass. *J. Sediment. Res.*, **85**, 1058–1081.

Su, M., **Lin, Z.**, **Wang, C.**, **Kuang, Z.**, **Liang, J.**, **Chen, H.**, **Liu, S.**, **Zhang, B.**, **Luo, K.**, **Huang, S.** and **Wu, Q.** (2020) Geomorphologic and infilling characteristics of the slope-confined submarine canyons in the Pearl River Mouth Basin, northern South China Sea. *Mar. Geol.*, **424**, 106166.

Talling, P.J., **Cartigny, M.J.B.**, **Pope, E.**, **Baker, M.**, **Clare, M.A.**, **Heijnen, M.**, **Hage, S.**, **Parsons, D.R.**, **Simmons, S.M.**, **Paull, C.K.**, **Gwiazda, R.**, **Lintern, G.**, **Hughes Clarke, J.E.**, **Xu, J.**, **Silva Jacinto, R.** and **Maier, K.L.** (2023) Detailed monitoring reveals the nature of submarine turbidity currents. *Nat. Rev. Earth Environ.*, **4**, 642–658.

Taviani, M., **Foglini, F.**, **Castellan, G.**, **Montagna, P.**, **McCulloch, M.T.** and **Trotter, J.A.** (2023) First assessment of anthropogenic impacts in submarine canyon systems off southwestern Australia. *Sci. Total Environ.*, **857**, 159243.

Taylor, W.J., **Hodgson, D.M.**, **Peakall, J.**, **Kane, I.A.**, **Morris, E.A.** and **Flint, S.S.** (2024a) Unidirectional and combined transitional flow bedforms: controls on process and distribution in submarine slope settings. *Sedimentology*, **71**, 1329–1362.

Taylor, W.J., **Hodgson, D.M.**, **Peakall, J.**, **Kane, I.A.**, **Flint, S.S.** and **Bouwmeester, M.J.** (2024b) Evolution and architecture of an overbank in an ocean-facing canyon-fill. https://doi.org/10.31223/X5CQ5Z.

Tek, D.E., **McArthur, A.D.**, **Poyatos-Moré, M.**, **Colombera, L.**, **Patacci, M.**, **Craven, B.** and **McCaffrey, W.D.** (2021) Relating seafloor geomorphology to subsurface architecture: how mass-transport deposits and knickpoint-zones build the stratigraphy of the deep-water Hikurangi Channel. *Sedimentology*, **68**, 3141–3190.

Tian, H., **Lin, C.**, **Zhang, Z.**, **Li, H.**, **Zhang, B.**, **Zhang, M.**, **Liu, H.** and **Jiang, J.** (2021) Depositional architecture, evolution and controlling factors of the Miocene submarine canyon system in the Pearl River Mouth Basin, northern South China Sea. *Mar. Pet. Geol.*, **128**, 104990.

Tinterri, R. (2011) Combined flow sedimentary structures and the genetic link between sigmoidal-and hummocky-cross stratification. *GeoActa*, **10**, 1–43.

Tsuji, T., **Ashi, J.** and **Ikeda, Y.** (2014) Strike-slip motion of a mega-splay fault system in the Nankai oblique subduction zone. *Earth Planets Space*, **66**, 120.

Vetter, E.W., **Smith, C.R.** and **De Leo, F.C.** (2010) Hawaiian hotspots: enhanced megafaunal abundance and diversity in submarine canyons on the oceanic islands of Hawaii. *Mar. Ecol.*, **31**, 183–199.

Von der Borch, C.C., **Grady, A.E.**, **Aldam, R.**, **Miller, D.**, **Neumann, R.**, **Rovira, A.** and **Eickhoff, K.** (1985) A large-scale meandering submarine canyon: outcrop example from the late Proterozoic Adelaide Geosyncline, South Australia. *Sedimentology*, **32**, 507–518.

Walker, R.G. (1975) Generalized facies models for resedimented conglomerates of turbidite association. *Bull. Geol. Soc. Am.*, **86**, 737–748.

Wang, X., **Wang, Y.**, **He, M.**, **Chen, W.**, **Zhuo, H.**, **Gao, S.**, **Wang, M.** and **Zhou, J.** (2017) Genesis and evolution of the mass transport deposits in the middle segment of the Pearl River canyon, South China Sea: Insights from 3D seismic data. *Mar. Pet. Geol.*, **88**, 555–574.

Wood, G.D., **Gabriel, A.M.** and **Lawson, J.C.** (1996) Palynological techniques – processing and microscopy. In: *Palynology: Principles and Applications* (Eds Jansonius, J. and MaxGregor, D.C.), pp. 29–50. American Association of Stratigraphic Palynologists Foundation, Dallas.

Wu, J.E., **McClay, K.**, **Whitehouse, P.** and **Dooley, T.** (2009) 4D analogue modelling of transtensional pull-apart basins. *Mar. Pet. Geol.*, **26**, 1608–1623.

Wu, N., **Nugraha, H.D.**, **Zhong, G.** and **Steventon, M.J.** (2022) The role of mass-transport complexes in the initiation and evolution of submarine canyons. *Sedimentology*, **69**, 2181–2202.

Wynn, R.B., **Piper, D.J.W.** and **Gee, M.J.R.** (2002) Generation and migration of coarse-grained sediment waves in turbidity current channels and channel-lobe transition zones. *Mar. Geol.*, **192**, 59–78.

Zhu, M., **Graham, S.**, **Pang, X.** and **McHargue, T.** (2010) Characteristics of migrating submarine canyons from the middle Miocene to present: implications for paleoceanographic circulation, northern South China Sea. *Mar. Pet. Geol.*, **27**, 307–319.

Supporting Information

Additional information may be found in the online version of this article:

Fig. S1. (A) Perinoid dinoflagellate cyst, *Cribroperidinium* sp., from sample PBI 1; England finder coordinate T19-2. (B) Gonyaulacoid cyst, *Oligosphaeridium complex*, from sample PBI 1; England finder coordinate U26-4.